

# Mapping the Local Interstellar Medium with High-Resolution UV Absorption Spectroscopy

by

Craig Malamut

Advisor: Dr. Seth Redfield

A thesis submitted to the  
faculty of Wesleyan University  
in partial fulfillment of the requirements for the  
Degree of Master of Arts  
in Astronomy

# Acknowledgments

The biggest thanks goes to my advisor Seth Redfield. Seth's guidance these past two years has enabled me to grow as a researcher and think like a scientist. His contagious enthusiasm and endless patience have made him an extraordinary teacher.

Thank you to Jeff Linsky, who provided expert advice throughout the process. Thank you to Brian Wood, who produced the Ly $\alpha$  fits of  $\lambda$  And and to Tom Ayres for his assistance in diagnosing possible wavelength calibration errors. Thank you to Meredith Hughes for sharing her knowledge of 49 Cet and HD141569 and to Roy Kilgard for his assistance with all my technical and programming woes. To Bill Herbst, Ed Moran, and the aforementioned Wesleyan professors, thank you for five great years of astronomy.

And I can't forget Team Redfield! Adam Jensen always provided great feedback and advice. Katy Wyman and Jakob Schaeffer may have graduated, but their presence was certainly felt. To Raquel and Diana, it's been a pleasure mastering astronomy with you. Thank you for your help throughout the process.

To my parents, thank you for your tremendous support throughout this year (and my entire life). You always encouraged me to do what I loved and to do it the best I can. I think this work reflects that.

I acknowledge support for this project through NASA HST Grant GO-11568 awarded by the Space Telescope Science Institute, which is operated by the Association of Universities for Research in Astronomy, Inc., for NASA, under contract NAS 5-26555, and a student research fellowship from the Connecticut Space Grant Consortium.

# Abstract

Observations using the Space Telescope Imaging Spectrograph aboard the *Hubble Space Telescope* have provided high-resolution near ultraviolet (UV) spectra showing MgII, FeII and MnII absorption due to the local interstellar medium (LISM). Spectra were analyzed towards 34 stars within 100 parsecs and across a wide range of spectral types. Observations span the entire sky, probing previously unobserved regions of the LISM. The heavy ions studied in this survey produce narrow absorption features that make possible the identification of multiple interstellar components. Simultaneous fits of the MgII, FeII, and MnII multiplets reveal anywhere from one to six individual absorption components in a particular sight line, where the number of absorbers roughly correlates with the length of the sight line. The simultaneous fitting procedure reduces the systematic errors involved in continuum placement and in determining the number of absorbers. Sight lines show evidence of previously unidentified clouds within the Local Bubble. These measurements will be added to a growing data set of 81 near UV sight lines. The increase in the number of sight lines will test and improve a three-dimensional dynamical model of the local interstellar medium. With an improved understanding of the LISM's kinematical structure, it will be possible to distinguish blended components within the absorption features of lighter ions. Specifically, the MAST Archive contains far UV observations of interstellar absorption by low mass ions (DI, CII, NI, OI) along the same sight lines. The combination of these data will constrain properties of the LISM such as temperature, turbulence, ionization, abundances and depletions.

# Contents

<b>1</b>	<b>Introduction</b>	<b>1</b>
1.1	The Earliest Investigations of the ISM . . . . .	1
1.2	The Local Interstellar Medium . . . . .	3
1.2.1	Observing the Warm Ionized Medium in the LISM . . . . .	5
<b>2</b>	<b>Observations and Data Reduction</b>	<b>8</b>
2.1	A SNAPSHOT Survey with STIS . . . . .	8
2.2	Data Reduction . . . . .	11
<b>3</b>	<b>The Fitting Procedure and Its Results</b>	<b>15</b>
3.1	Fitting the Continuum . . . . .	15
3.2	Fitting the ISM Features . . . . .	18
3.3	Determining Uncertainty . . . . .	20
3.4	Upper Limits . . . . .	21
3.5	Fits . . . . .	21
3.6	Results . . . . .	39
3.7	Final Fit Parameters . . . . .	40
<b>4</b>	<b>Analysis of the LISM Sample</b>	<b>44</b>
4.1	The Velocity Distribution . . . . .	44

4.2	The Doppler Parameter Distribution . . . . .	47
4.3	The Column Density Distribution . . . . .	49
4.4	Number of Components Versus Distance . . . . .	49
<b>5</b>	<b>Discussion</b>	<b>53</b>
5.1	Comparison with Dynamical Model . . . . .	53
5.2	Finer Details . . . . .	56
5.3	Temperature and Turbulence . . . . .	57
5.4	Astrospheres . . . . .	59
5.5	Circumstellar Disks . . . . .	61
5.5.1	Sight lines towards stars with CS disks . . . . .	63
5.5.2	Sight lines near a star with a CS disk . . . . .	65
<b>6</b>	<b>Conclusions</b>	<b>66</b>
6.1	Future Work . . . . .	67
	<b>Bibliography</b>	<b>69</b>

# List of Tables

2.1	Parameters for Stars in LISM SNAP Program <sup>a</sup> . . . . .	9
3.1	Fit Parameters for MgII LISM Components within 100 pc . . . . .	41
3.2	Fit Parameters for FeII LISM Components within 100 pc . . . . .	42
3.3	Fit Parameters for MnII LISM Components within 100 pc . . . . .	43
4.1	Mean Values for Doppler Parameter and Log Column Density . . . . .	47
5.1	Comparison with Dynamical Model . . . . .	55

# Chapter 1

## Introduction

The local interstellar medium (LISM) consists of the diffuse material that engulfs the solar system as well as thousands of nearby stars. To observe anything beyond our solar system, we must peer through this interstellar material. As Frisch et al. (2011) describe it, the LISM is the “screen through which we view the rest of the Universe.” Even more, the LISM offers the unique opportunity to study the interstellar medium (ISM) in remarkable detail. We can extend our knowledge of its small-scale behavior to similar regions in distant ISM within the galaxy and beyond. The LISM provides insight into the history of our neighborhood in the Milky Way and allows us to contextualize our solar system and stellar systems surrounding us.

### 1.1 The Earliest Investigations of the ISM

The concept of interstellar space may have entered public discourse as far back as the 17th century, when Francis Bacon acknowledged the “interstellar skie” in his 1627 *Sylva Sylvarum: Or Naturall Historie. In Ten Centuries* (Figure 1.1). Some of the first published detections of interstellar absorption, however, appeared three centuries later when Hartmann (1904) observed a “sharp,” unmoving calcium feature amidst the oscillating lines of the spectroscopic binary system  $\delta$  Orionis. Hartmann deduced that the feature was the result of calcium gas that lay between

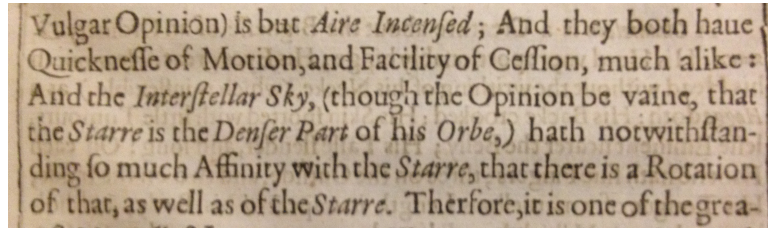


**Figure 1.1:** One of the earliest mentions of interstellar space from Francis Bacon’s *Sylva Sylvarum: Or Naturall Historie. In Ten Centuries* (Courtesy of Special Collections & Archives, Olin Library, Wesleyan University, Middletown, CT) (Bacon 1626).

us and  $\delta$  Orionis and even provided its projected velocity. Hartmann’s discovery was followed by detections of interstellar sodium (Heger 1919), and the analysis of more complicated sight lines with multiple interstellar absorption components (Beals 1936).

The advent of sounding rockets enabled astronomers to capture ultraviolet spectra, containing a vast array of strong interstellar transition lines. Morton & Spitzer (1966) were the first to exploit this technology for far UV spectroscopy of the ISM, detecting OI, SiII, AlII, CII, and CIV consistent with HI clouds along their sight lines towards  $\delta$  and  $\pi$  Scorpii. In the following decade, the *Copernicus* satellite launched, which contained a UV telescope and X-ray detectors. *Copernicus* led to a detailed survey of elemental abundances in the ISM (Cowie & Songaila 1986; Jenkins 1987). Following *Copernicus*, the *International Ultraviolet Explorer (IUE)* was launched in a joint effort by NASA, the European Space Agency (ESA), and the United Kingdom’s Science and Engineering Research Council. Though they did not provide improved spectral resolution, the two UV spectrographs aboard *IUE* operated for 18 years and led to advances in a number of ISM research areas such as the study of interstellar dust (Mathis 1987) and the distribution of highly ionized ISM (Sembach & Savage 1992).

The most recent leaps in space-based UV telescopes came with the launch of

the *Hubble Space Telescope* (*HST*). Initially, *HST* was equipped with the Goddard High-Resolution Spectrograph (GHRS). GHRS provided unprecedented spectral detail, allowing for far greater precision in the analysis of narrow ISM absorption. In 1997, GHRS was replaced by the Space Telescope Imaging Spectrograph (STIS), which incorporated more advanced digital cameras capable of broad spectral coverage in a single echelle exposure (Ayres 2010). Today, STIS remains the best instrument for high-resolution UV spectroscopy currently available.

## 1.2 The Local Interstellar Medium

In their 1977 paper, McKee & Ostriker describe a three phase model of the interstellar medium. The first phase, known as the hot ionized medium (HIM), consists of hot, tenuous gas that fills the largest fraction of interstellar space. Temperatures of this material reach  $\sim 10^6$  K with a density ( $n$ ) of  $\sim 10^{-2.5}$  cm $^{-3}$ . Heating mechanisms for the HIM include energetic particles from stellar winds, compact X-ray sources, and supernova shockwaves (McCray 1987). Embedded in the HIM are cold, dense regions known as cold neutral medium (CNM) ( $T \sim 100$  K,  $n \sim 100$  cm $^{-3}$ ). Surrounding the CNM is an intermediary region of warm material ( $T \sim 8000$  K,  $n \sim 0.5$  cm $^{-3}$ ). The gas may be partially ionized (WIM) or neutral (WNM) depending on how well it is shielded from various heating sources.

The Sun and nearby stars reside in a region of HIM known as the Local Bubble. The first evidence for this hot cavity came from color excess maps indicating a large pocket in the dust surrounding the solar system and observations of diffuse soft X-ray background observed across the entire sky (Frisch et al. 2011 and references therein). The edge of the Local Bubble can be traced by the onset of NaI and CaII absorption, indicators of colder material. This edge begins anywhere from 65 to

250 pc depending on the observed direction (Sfeir et al. 1999). The carving of the Local Bubble is likely the result of stellar winds or supernova explosions. Figure 1.2 shows a map of the Local Bubble produced by observing NaI absorption in 311 sight lines within  $\sim 350$  pc of the Sun (Lallement et al. 2003).

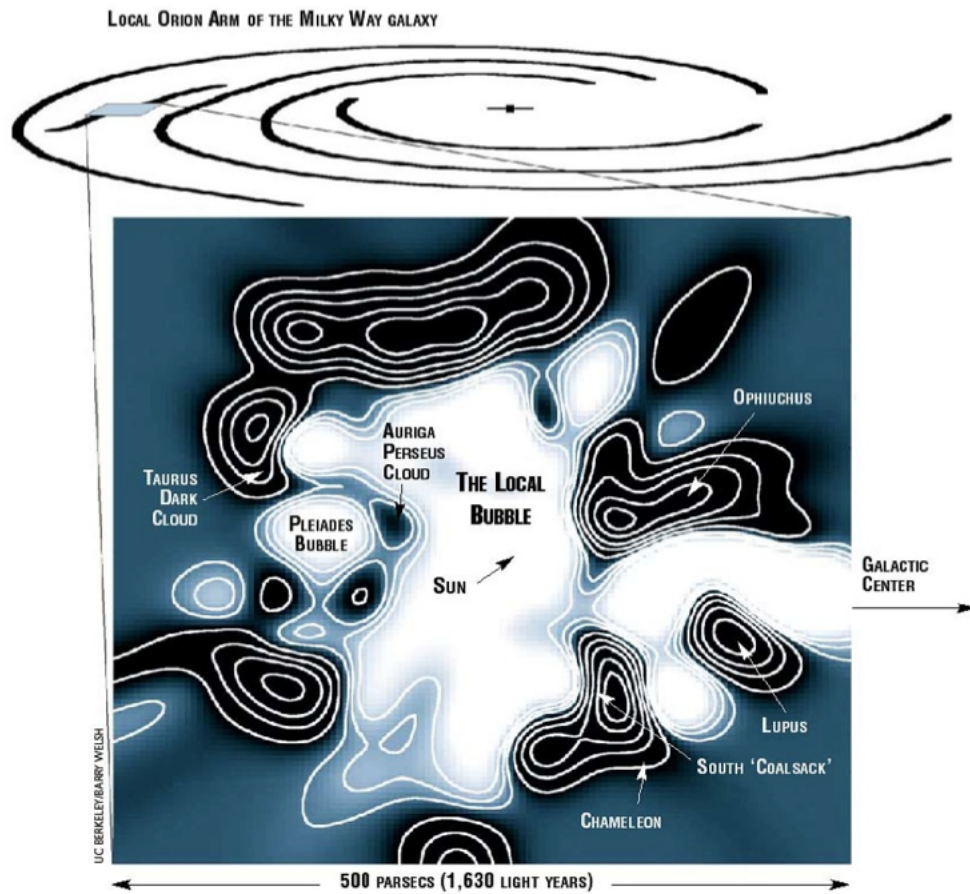


**Figure 1.2:** A map by Lallement et al. (2003) of the Local Bubble with contours denoting increasing density. The white regions represent the HIM of the Local Bubble, while the darker regions are CNM that trace its borders.

### 1.2.1 Observing the Warm Ionized Medium in the LISM

Within the Local Bubble, we observe clouds of warm gas. Observations of the LISM suggest this warm interstellar material exists in discrete clouds, each distinguished by its unique properties (e.g., density, temperature, projected velocity). The predominant approach to study the LISM is to observe its absorption signature against bright, nearby background sources. The shape and position of absorption features offer insight into the nature of the ISM along a particular line of sight. Most resonance lines of common ions in the ISM exist in the UV.

With the advent of space-based high-resolution UV spectrographs largely thanks to *HST*, the warm material in the LISM has been studied in unprecedented detail. The proximity of this interstellar material allows for detailed study currently impossible for longer distance scales. When observed at distance scales of hundreds to thousands of parsecs, transition lines of ions in the ISM are often blended and saturated. By observing nearby stars, the shapes of the absorption lines are frequently more discernible, allowing us to identify and characterize the constituent clouds of the LISM.

The observation of heavier elements pervasive in warm clouds has proven to be a boon to our understanding of the structure of the LISM. Their relatively large masses reduce thermal broadening and blending of line profiles, allowing for more precise measurement of cloud velocities and easier identification of multiple clouds along a line of sight. Of particular use are MgII and FeII, both of which have high cosmic abundance and are the dominant ionization stages in the LISM (Slavin & Frisch 2008). Both produce multiplet features that provide independent measurements of each ion along the line of sight. Genova et al. (1990) pioneered much of this work when they used *IUE* to observe the MgII *h* and *k* lines of cool

stars within 30 pc of the Sun. ISM absorption superimposed on chromospheric emission hinted at heterogeneities in the column density distribution of MgII as well as unresolved clouds beyond the “Local Cloud.” Later studies using GHRS identified the two nearest clouds—the Local Interstellar Cloud and the Galactic Cloud—and established a velocity vector with only  $\sim 10$  lines of sight (Lallement & Bertin 1992; Lallement et al. 1995).

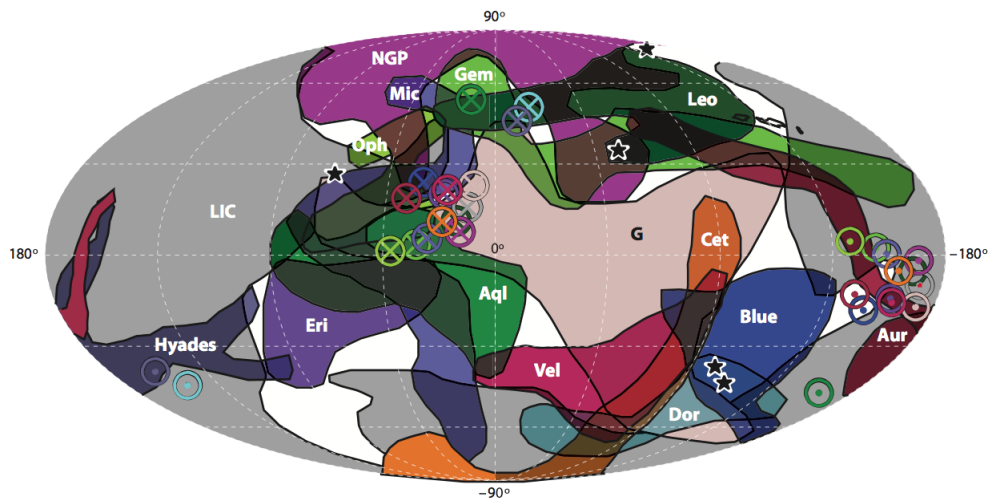


**Figure 1.3:** The angular extent of 15 LISM clouds determined through the triangulation of cloud velocities towards 157 stars within 100 pc (Redfield & Linsky 2008). A circled  $\times$  denotes the heliocentric upwind velocity of a cloud, while a circumpunct signifies the downwind direction. The black stars are sight lines of radio scintillation sources identified by Linsky et al. (2008).

Redfield & Linsky (2002) continued these types of observations with STIS, including MgII and FeII in their survey. Their more extensive and higher precision data set has led to the identification of 15 clouds (Figure 1.3) each with a unique velocity vector (Redfield & Linsky 2008). Observations of multiple ions and ionization levels in these clouds have enabled measurements of ionization structure (Wood et al. 2002), abundances and depletions (Redfield & Linsky 2004a), and temperature and turbulence (Redfield & Linsky 2004b). Furthermore, increased

---

numbers of sight lines have made it possible to examine the small-scale structure of the LIC (Redfield & Linsky 2001). The goal of this study is to build on this body of research by adding a large number of observations of heavy ions along more distant sight lines, thereby extending and refining measurements of the LISM.

# Chapter 2

## Observations and Data Reduction

### 2.1 A SNAPSHOT Survey with STIS

The data were obtained by the Space Telescope Imaging Spectrograph (STIS) on board the *Hubble Space Telescope* (*HST*). STIS offers high resolution UV and optical spectroscopy, making it a valuable tool for detecting the narrow absorption lines of the warm ionized LISM. STIS has a far UV (FUV) channel (1150 – 1700 Å), a near UV (NUV) channel (1600 – 3100 Å), and an optical channel ( $\sim 2000$  – 10,000 Å). These observations required the NUV channel, known as STIS/NUV-MAMA, which uses a Cs<sub>2</sub>Te Multi-Anode Microchannel detector Array (MAMA). Its field of view is 25''  $\times$  25'' and it has a plate scale of 0.025 arcsec/pixel. For this research, observations were taken with the E230H echelle, centered at 2713 Å. The spectral resolving power is  $R \sim 114,000$  (where  $R \equiv \frac{\lambda}{\Delta\lambda}$ ) with a spectral range of  $\sim 200$  Å. This broad spectral range encompasses all of the lines concerned in this study, namely, MgII (2796.3543 Å and 2803.5315 Å), FeII (2586.6500 Å and 2600.1729 Å), and MnII (2594.499 Å and 2606.462 Å).

For this research, a SNAPSHOT survey was used to capture spectra for 36 sight lines towards stars within 100 pc (Figure 2.1). The SNAP program is designed to have short exposures on hand to observe in between other observations. The observation times, including overhead times, are limited to <45 minutes. These

Table 2.1. Parameters for Stars in LISM SNAP Program<sup>a</sup>

HD No.	Other Name	Spectral Type	$m_V$ (mag)	$v_R$ (km s <sup>-1</sup> )	$l$ (deg)	$b$ (deg)	Distance (pc)	$S/N$ (MgII)	$S/N$ (FeI)	$S/N$ (MnII)	Other Spectra
209100	$\epsilon$ Ind	K5V	4.833	-40.4	336.2	-48.0	3.63	18.3	6.1	4.2	GHRSEch-A (Ly $\alpha$ )
115617	61 Vir	G5V	4.74	-8.5	311.9	44.1	8.53	10.2	5.3	7.1	STIS/E140M E230M
114710	$\beta$ Com	G0V	4.311	6.1	43.5	85.4	9.15	12.8	8.4	8.6	FUSE
	WD1620-391	DA	10.974	43.2 <sup>b</sup>	341.5	7.3	13.2	5.3	6.3	6.5	GHRSE/G160M, FUSE
72905	$\pi^1$ UMa	G1.5V	5.706	-12.0	150.6	35.7	14.6	12.2	7.3	7.0	FUSE
217014	51 Peg	G5V	5.524	-31.2	90.1	-34.7	15.4	4.6	4.8	5.8	STIS/G140M (Ly $\alpha$ ), FUSE
120136	$\tau$ Boo	F7V	4.541	-15.6	358.9	73.9	15.6	12.0	8.8	10.2	STIS/G140M (Ly $\alpha$ )
142373	X Her	F9V	4.672	-55.4	67.7	50.3	15.9	8.4	6.8	12.4	STIS/E140M
220140	V368 Cep	G9V	7.622	-16.8	118.5	16.9	19.7	13.4	3.7	1.9	GHRSE/G140M G160M G270M
97334	MN UMa	G0V	6.476	-2.6	184.3	67.3	21.7	10.4	4.1	3.7	STIS/E140M E230M
	WD1337+705	DA	12.8	26	117.2	46.3	24.8	2.4	3.4	3.4	STIS/G430M, FUSE
222107	$\lambda$ And	G8III-IV	3.975	6.8	109.9	-14.5	25.8	29.6	7.4	5.8	GHRSEch-A (Ly $\alpha$ ), FUSE
180711	$\delta$ Dra	G9III	3.188	24.8	98.7	23.0	30.7	12.0	4.6	4.7	FUSE
12230	47 Cas	F0V	5.26	-26	127.1	15.0	33.6	10.8	14.0	15.9	GHRSE/G140M, FUSE
163588	$\xi$ Dra	K2III	3.867	-26.4	85.2	30.2	34.2	16.8	3.0	2.6	FUSE
216228	$\iota$ Cep	K0III	3.621	-12.6	111.1	6.2	35.4	17.6	5.2	4.8	FUSE
93497	$\mu$ Vel	G5III	2.818	6.2	283.0	8.6	35.5	23.2	9.4	8.2	STIS/E140M, FUSE
149499	V841 Ara	K0V	8.737	-24.8	329.9	-7.0	37.1	4.4	1.1	0.8	STIS/E140M, FUSE
131873	$\beta$ UMi	K4III	2.238	17.0	112.6	40.5	38.8	20.7	2.8	2.3	FUSE
210334	AR Lac	G2IV	6.203	-34.6	95.6	-8.3	42.0	10.7	4.7	4.3	GHRSE/G160M G270M, FUSE
28911	HIP21267	F5V	6.619	35	183.4	-22.6	43.9	8.8	6.6	9.0	FUSE
28677	85 Tau	F4V	6.02	36	180.9	-21.4	44.9	10.4	10.4	14.3	FUSE
204188	IK Peg	A8	6.06	-11.4	70.4	-22.0	46.0	6.2	8.3	12.5	GHRSE/G160M, FUSE
	WD0549+158	DA	13.06	12.0	192.0	-5.3	49	3.5	4.5	4.8	STIS/G140M G230M, FUSE
9672	49 Cet	DA	13.14	-26.5	336.6	-32.9	58	2.9	4.0	4.2	FUSE
43940	HIP29852	A2V	5.62	12.1 <sup>c</sup>	166.3	-74.8	61.3	20.0	30.3	32.4	FUSE
137333	$\rho$ Oct	A2V	5.57	-11	307.0	-23.0	62.1	14.1	22.2	26.2	FUSE
	WD1631+781	DA	13.03	-11	111.3	33.6	67	0.1	0.1	0.1	FUSE
3712	$\alpha$ Cas	K0II-III	2.377	-4.3	121.4	-6.3	70.1	18.8	4.8	4.3	FUSE
149382	HIP81145	B5	8.872	3	11.8	27.9	76.5	15.7	18.9	21.1	FUSE
149730	R Ara	B9IV/V	11.99	40.5 <sup>b</sup>	245.4	-21.4	78	6.1	8.3	9.0	FUSE
	IX Vel	O9	6.73	20	330.4	-6.8	80.4	10.0	14.6	16.2	FUSE
75747	RS Cha	A7V	9.503	26.0	264.9	-7.9	96.3	6.8	8.6	9.4	STIS/E140M, FUSE
141569	HIP77542	B9	7.143	-7.6 <sup>e</sup>	282.6	-21.6	97.8	5.9	10.7	14.0	STIS/E230M, FUSE
					4.2	36.9	99.0	8.1	10.4	12.2	FUSE

<sup>a</sup>All stellar parameters taken from the SIMBAD database unless otherwise stated.<sup>b</sup>Holberg et al. (1998)<sup>c</sup>Hughes et al. (2008)<sup>d</sup>Gontcharov (2006)<sup>e</sup>Dent et al. (2005)

observations necessitated 20 minutes of preparation time, leaving a maximum on-target exposure time of 25 minutes. The 90 potential targets proposed for the SNAP survey were partly selected on the basis that they were bright enough to achieve the necessary signal-to-noise ratio ( $S/N$ ) in under 25 minutes. They were also selected to be broadly distributed throughout the sky. Their broad distribution allowed *HST* to have targets readily available to increase efficiency. After the SNAP program culminated, the spectra captured had an average  $S/N$  of 11.3, 8.8, and 9.8 for MgII, FeII, and MnII respectively. The  $S/N$  was calculated by averaging the flux divided by its error over the  $\sim\pm 50$  km s<sup>-1</sup> region surrounding each line. This method includes the absorption feature in the calculation, so the  $S/N$  may be underestimated. For a full list of the observed targets, see Table 2.1.

Two sight lines in the sample could not be fit. The  $\beta$  UMi sight line could not be analyzed because its strong stellar wind produced a dramatic P Cygni profile (Figure 2.2). A P Cygni profile is the result of an outflow of material from the star. Material moving towards the observer creates strong absorption blue-shifted relative to the star's velocity. Although this profile provides a wealth of information about the stellar wind, it also prevents any confident placement of a continuum and obscures ISM features. The WD1631+781 sight line was removed from the sample because it had far too low  $S/N$ , possibly due to inaccurate pointing.

The ions in this survey were chosen to complement data archived in the Mikulski Archive for Space Telescopes (MAST). All of the NUV observations were along sight lines previously observed in the FUV and made available in the MAST archive. The FUV spectra contains absorption from lighter ions such as DI, CII, NI, and OI, but these features are intrinsically broad and frequently saturated. The narrow absorption lines make it possible to understand the kinematic structure, and this information, in turn, can be used to identify the blended and satu-

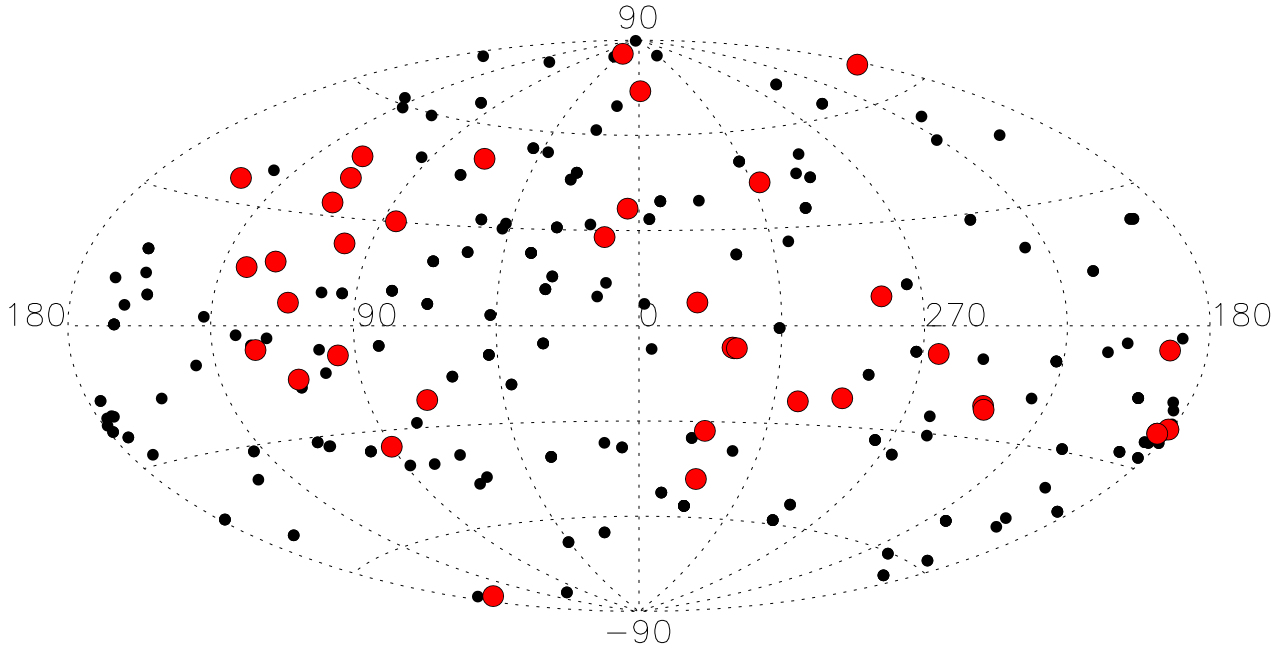


**Figure 2.1:** Galactic coordinates of all sight lines for which LISM spectra have been obtained. Red circles indicate sight lines added by this *HST* SNAPSHOT survey. The three pairs of stars with small angular separation in the bottom right quadrant offer an opportunity to probe small scale changes in LISM clouds.

rated LISM components in the MAST FUV spectra.

## 2.2 Data Reduction

The NUV/MAMA detector is a photon counting detector that produces a two-dimensional UV image. Figure 2.3 shows an example of the raw data for HD 141569. The image contains all of the E230H echelle orders stacked verti-

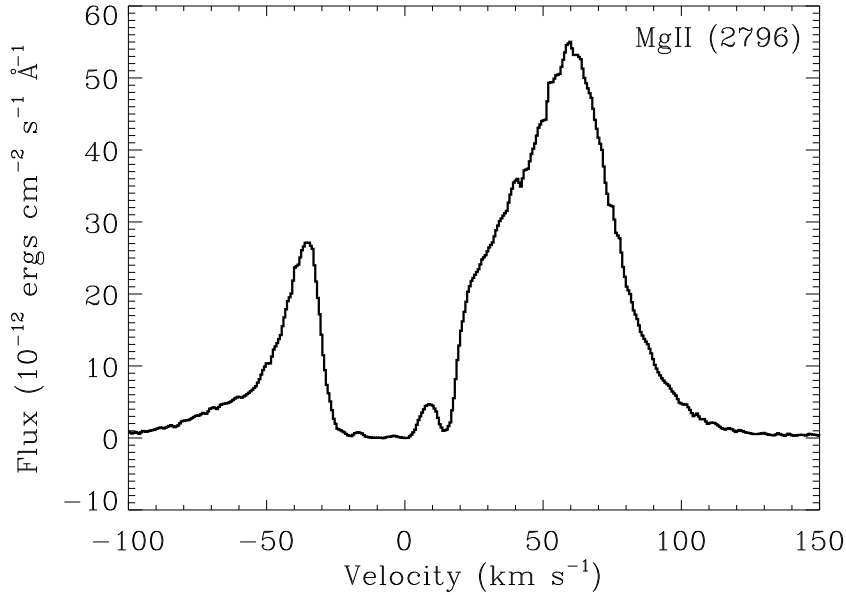


**Figure 2.2:** The 2796 Å line of  $\beta$  UMi shows a P Cygni profile. The strong absorption prevents confident continuum placement and ISM identification. The narrow absorption feature at 15 km s<sup>-1</sup> may be ISM, but the unreliable continuum placement would have significant effects on the parameters of the profile.

cally. The dark patches in the spectra at the top and bottom of the image are due to interstellar MgII, FeII, and MnII transition lines. The Space Telescope Science Institute (STScI) `calstis` pipeline performs a number of tasks on this two-dimensional image such as linearity correction, flat field correction and dark subtraction. It flags bad pixels, corrects for cosmic rays and scattered light, and converts to a heliocentric reference frame. In order to translate pixels on the detector into wavelengths, internal Pt-Cr/Ne line lamps are used contemporaneously to provide a reference spectrum for calibration. The `calstis` pipeline returns a number of one-dimensional arrays including flux, wavelength and error arrays for each order.

Once the data goes through the STIS reduction pipeline, a second pipeline is utilized to perform a series of finer calibrations. Using 3184 echelle observations of

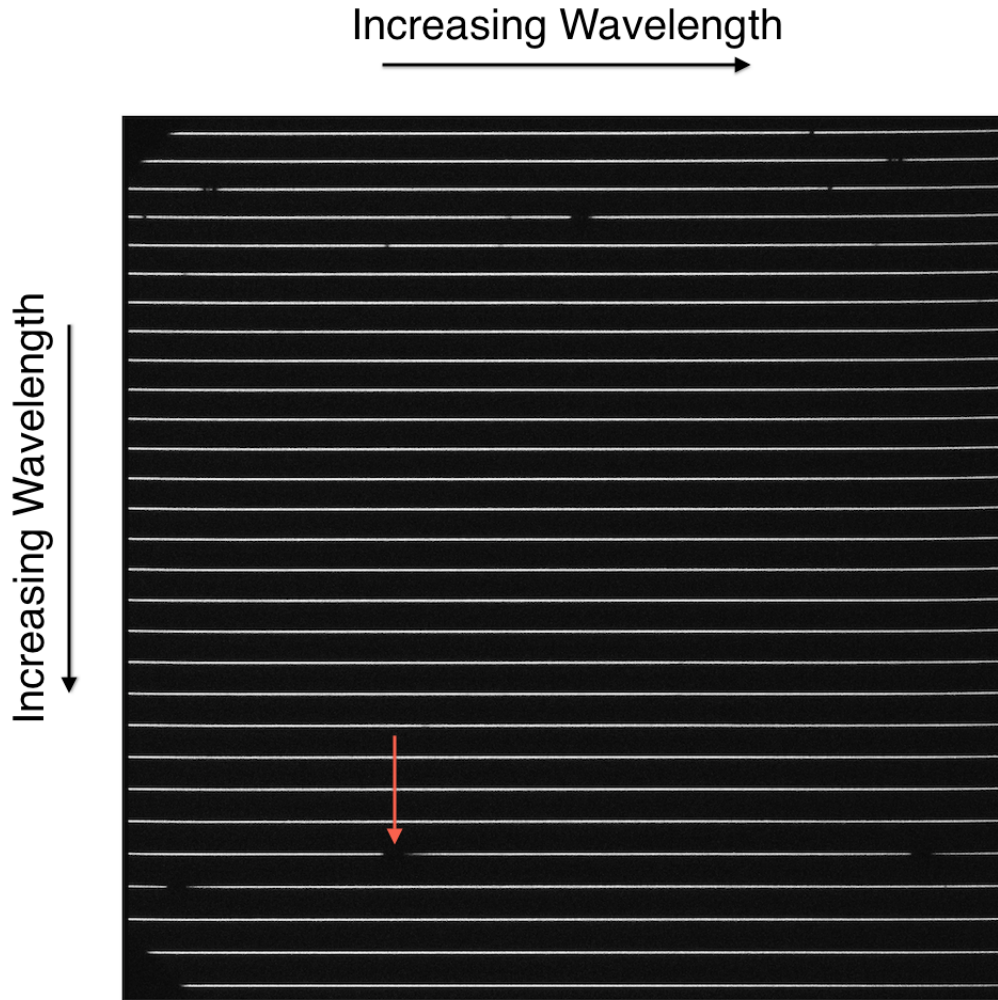


**Figure 2.3:** Raw STIS spectra towards HD 141569, the longest sight line in the sample. Each horizontal, white line is an echelle order with wavelength increasing left to right within the order and top to bottom between orders. The dark pixels have count values as low as 0 and the brightest pixels have count values as high as  $\sim 90$ . Multiple components produce broad, saturated features that are visible as interruptions in the spectra. Towards the bottom of the image is the MgII doublet ( $2796 \text{ \AA}$ ,  $2803 \text{ \AA}$ ). The red arrow points to the  $2796 \text{ \AA}$  line. The  $2803 \text{ \AA}$  line, visible to the right on the same order, is repeated on the consecutive order. During the StarCAT reduction process, these orders are concatenated and duplicate information is averaged. The FeII and MnII absorption features are visible at the top of the image.

545 targets, Ayres (2010) produced a catalog of high resolution UV spectra with STIS called “StarCAT.” StarCAT corrects for distortions that persist when the

---

*HST* pipeline converts pixel coordinates in the raw MAMA frames to wavelengths. It improves on the ability of the `calstis` pipeline to flag poor quality data points. It then concatenates the various echelle orders, producing a one dimensional array containing the entire spectral range observed. Once the data runs through the StarCAT reduction process, it is ready to be fit.

# Chapter 3

## The Fitting Procedure and Its Results

Once the observations are collected and reduced, the fitting procedure can begin. Each sight line is simplified to a single flux and error array of over 46,000 data points corresponding to  $\sim 0.006$  Å increments in a wavelength array spanning 270 Å of the near UV. The spectra contain a wide range of features characteristic of the various spectral types observed. For example, the G stars in the sample display prominent MgII *h* and *k* emission features while the white dwarfs are relatively flat across the entire range. Consistent among all the spectra, however, are a number of deep, sharp absorption features: the imprint of the LISM.

### 3.1 Fitting the Continuum

The fitting procedure begins by fitting continua to the spectra. The continuum consists of the superposition of blackbody radiation from the star and any of its emission or absorption features. Oftentimes, the interstellar absorption is embedded in stellar features. Challenges arise when trying to distinguish ISM features from stellar features, especially when the stellar features are complicated. To match the expected continuum over the interstellar absorption, I use a number of techniques within the program `mkfb.pro` and elsewhere. The program `mkfb.pro`,

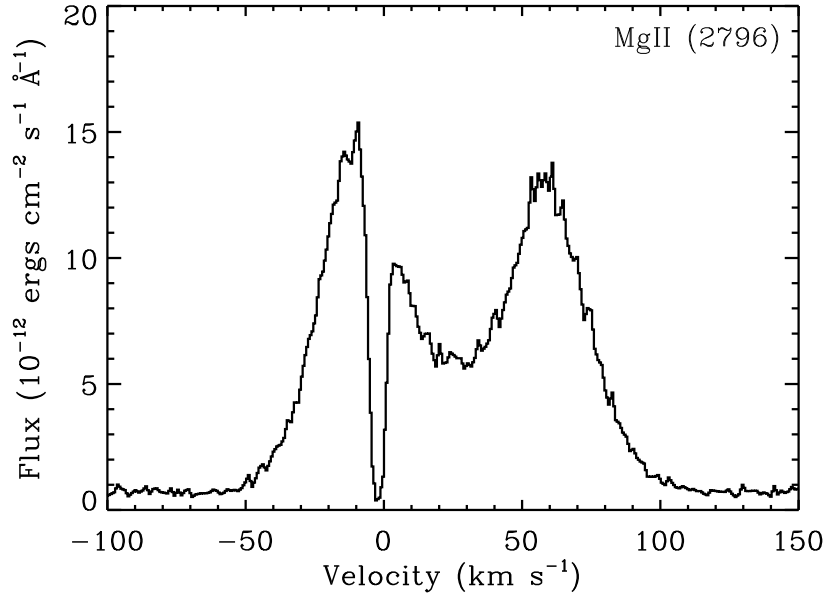


**Figure 3.1:** An ISM component embedded in the central reversal of the MgII  $k$  stellar emission line of  $\delta$  Dra. The ISM absorption feature at  $-2 \text{ km s}^{-1}$  is much narrower than the stellar feature. The ISM component is offset from the stellar feature which is centered at  $25 \text{ km s}^{-1}$ , indicating that it is independent of the stellar atmosphere.

written by S. Redfield, has been used in previous LISM studies (e.g., Redfield & Linsky 2002, 2004a).

The first step is identifying the interstellar absorption. A key feature is the shape of the line. Interstellar absorption for a particular ion in this survey is generally narrower than the stellar counterpart due to less dramatic broadening mechanisms in the ISM than in stellar atmospheres (Figure 3.1). Further, the stars in this survey are nearby and therefore most have known radial velocities (see Table 2.1). Because ISM clouds have independent radial velocities, their features are often offset from the stellar features.

Once the ISM features have been identified, they can be “ignored” in the continuum fitting procedure. Usually the first method of fitting the continuum is to use a polynomial fit. The program `mkfb.pro` performs a least-square polynomial

fit of order 1 to 10 within a selected range or set of ranges of the flux array. Flat or simple continua (e.g., WD1620-391 in Figure 3.4) can be fit with lower order polynomials, while more complex continua (e.g.,  $\iota$  Cep in Figure 3.10) can necessitate higher orders. Occasionally, the ISM features are embedded on one side of a symmetrical stellar feature (e.g., MgII towards  $\epsilon$  Ind in Figure 3.3), warranting the use of a flipped profile approach. A selected range of the flux array can be reversed and smoothed, laying the unblemished half of the stellar feature over the ISM components.

Fitting the continuum requires “bridging the gap” over ISM features. In every case, the data have some level of noise which cannot be accurately accounted for in the smooth polynomial and flipped profile fits. Systematic errors in the continuum fitting procedure can be mitigated using the “duplicate” information contained in the spectra. An important aspect of the MgII, FeII, and MnII ions selected for studying the ISM is that they have multiple resonance lines in the observed wavelength range. Therefore, two lines of a multiplet provide two independent measurements of the same ion along the same sight line. Because each line must contain the same components at the same number of Doppler-shifted wavelengths, they can be fit simultaneously with the corresponding components linked in velocity. One line has all of its parameters frozen, so that corresponding components are forced to have identical velocities, Doppler parameters and column densities. If a systematic deviation is observed in the simultaneous fit, it may highlight an issue with the continuum. When this occurs, a new continuum can be fit over the line to correct the inconsistency.

## 3.2 Fitting the ISM Features

Once a continuum has been estimated over the missing stellar flux, the fitting procedure can begin. Fitting consists of applying the maximum number of Voigt absorption profiles to the continuum that are statistically justified. Each justified Voigt profile represents a discrete interstellar component. A Voigt profile is the convolution of a Lorentzian profile and Gaussian profile, which together describe the natural and Doppler broadening mechanisms that shape ISM profiles.

Fitting begins by attempting to fit a particular line with the lowest number of components. Typically that is one component, but occasionally it is clear from visual inspection that there is more than one component (e.g., RS Cha in Figure 3.17, HD 141569 in Figure 3.19). Once the simplest fit is completed, another component is added, usually “improving” the fit by increasing the number of free parameters. At a certain point, however, adding more components does not significantly improve the fit. Figure 3.2 demonstrates this process of adding components to a fit. Adding a second and third component results in a better match to the data, but the addition of a fourth component shows no improvement.

To test whether or not an additional component significantly improves the fit, an F-Test is employed. An F-test is a statistical test that compares two fits to the same data. The fit with more free parameters should match the data better, but there must be sufficient reason to discount the null hypothesis. The null hypothesis states that the more complicated fit is not significantly better, and the F-test determines the likelihood that this hypothesis is true. The probability that the null hypothesis is correct is represented by an F-distribution. A cutoff is determined in this distribution at which there is only a 5% chance that the null hypothesis is correct. If the ratios of the reduced chi-squared ( $\chi^2_\nu$ ) values for the

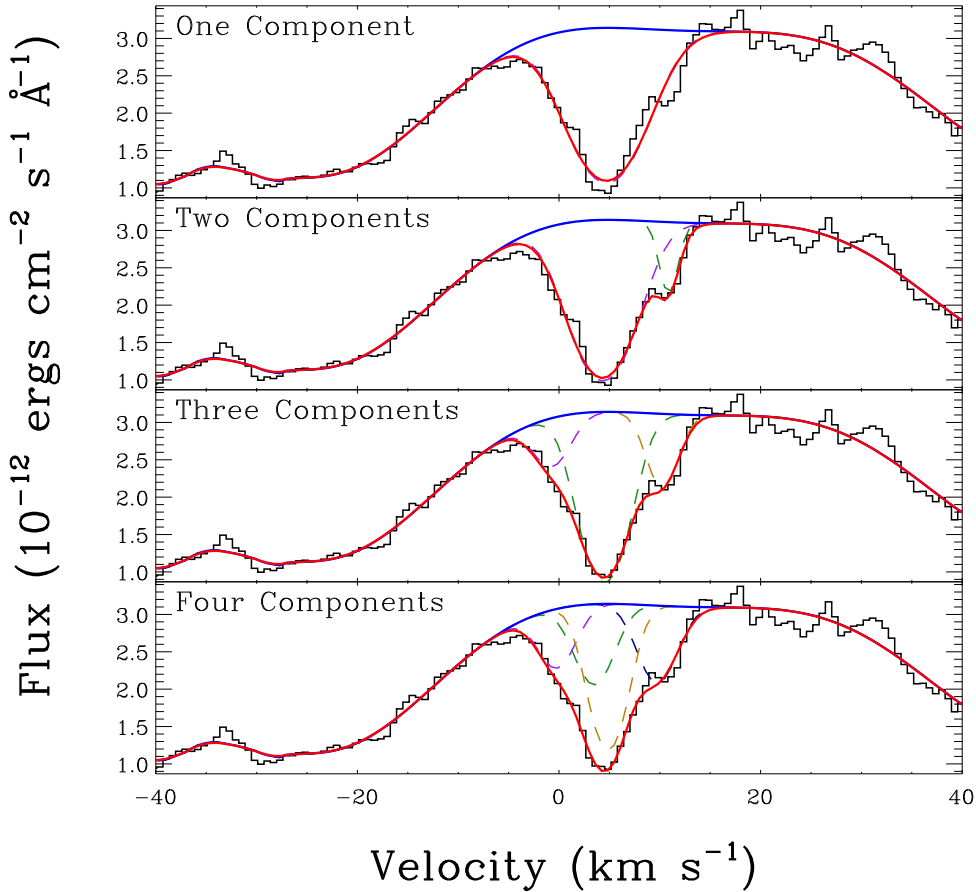


**Figure 3.2:** A series of fits to the FeII 2586 Å line of  $\lambda$  And using one to four components. An F-test determines that the three-component model is the best fit to the data. Note the marginal changes in fit from three components to four, while the improvements are apparent between one-, two- and three-component fits.

fits exceeds this cutoff, then the extra component is justified (Bevington 2003).

A Marquart  $\chi^2$  minimization technique is used to fit the absorption profiles. The program `gismfit.pro` (written by S. Redfield and B. Wood and used in previous LISM studies such as Redfield & Linsky 2002) varies the Doppler parameter, wavelength centroid, and column density around initial guesses until a minimum  $\chi^2_\nu$  value is achieved. If the guesses are very poor, the program will fit the line in a manner that may not make physical sense or seem unlikely in the context of our

understanding of ISM absorption profiles. In such cases, guesses must be altered and the program must be reran until a plausible fit is returned.

### 3.3 Determining Uncertainty

The uncertainty for each parameter is calculated using a Monte Carlo error analysis. A Monte Carlo method uses random inputs into a model to estimate an outcome probabilistically. As the number of random inputs increases, the approximation improves. This method is used when the model is too complicated to evaluate deterministically or when systematic errors dominate random errors. When fitting absorption features, the model varies many free parameters in order to accurately describe the data. When calculating uncertainty, parameter values are randomly generated based on a normal distribution around the initial guesses. How the distribution of outcomes compares to the data determines the uncertainty for each parameter.

For a particular ion, the fitting procedure is performed three times: once for each observed line of the multiplet and a third time for a simultaneous fit. Ideally, the three fits should justify the same number of components with the same parameters, but occasionally this is not the case. Usually, there are minor differences, but if the lines are largely blended or noisy, the differences may be substantial. These discrepancies highlight the uncertainty in the measurements. The final parameter values and their uncertainties seen in Tables 3.1, 3.2, and 3.3 are the weighted means of the parameters for the two individual fits and the simultaneous fit.

The simultaneous fitting procedure does not go beyond the two lines of a particular ion. Fitting FeII and MgII together, for example, would reduce their

independence and would prevent any meaningful comparison of the two ions along the sight line.

### 3.4 Upper Limits

In several cases, MgII absorption is detected, but a corresponding component is not observed in FeII or MnII. It is assumed that the MgII, FeII, and MnII in each cloud are well mixed, so an upper limit is calculated for the column density of a component hidden within the noise. To do so, I produce a series of Voigt profiles with various column densities, put them on a flat, normalized continuum, and approximate the area under the curve of each profile. I compare these values to the root mean square of the normalized data over the expected absorption region, and choose as the upper limit the column density of the largest profile that does not exceed three times the RMS (i.e., the  $3\sigma$  upper limit).

### 3.5 Fits

I was able to fit interstellar absorption in 34 lines of sight, with an average of 2.3 components per sight line. Every sight line contains MgII absorption, and 33 show FeII absorption as well. I was also able to fit MnII absorption along four lines of sight. In cases where no feature was detected in FeII or MnII but observed in MgII, I calculate upper limits for their column densities. The fits are displayed in Figures 3.3 – 3.19. The final parameters are listed in Tables 3.1, 3.2, and 3.3, with  $3\sigma$  upper limits preceded by a “less than” symbol.

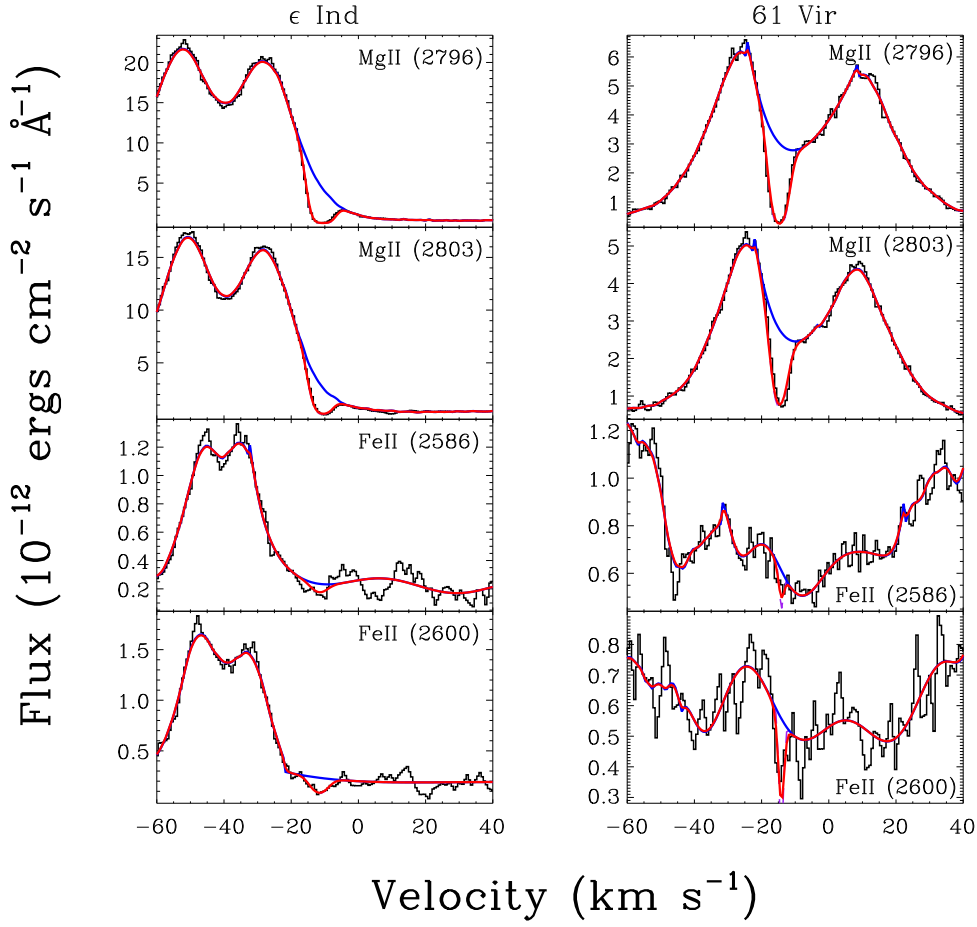


**Figure 3.3:** Simultaneous fits of MgII and FeII. Heliocentric velocities are provided along the x-axis. The solid blue line is the continuum fit. The dashed lines (visible in multi-component fits) are the profiles of each component. The solid red line is the superposition of all components onto the continuum.

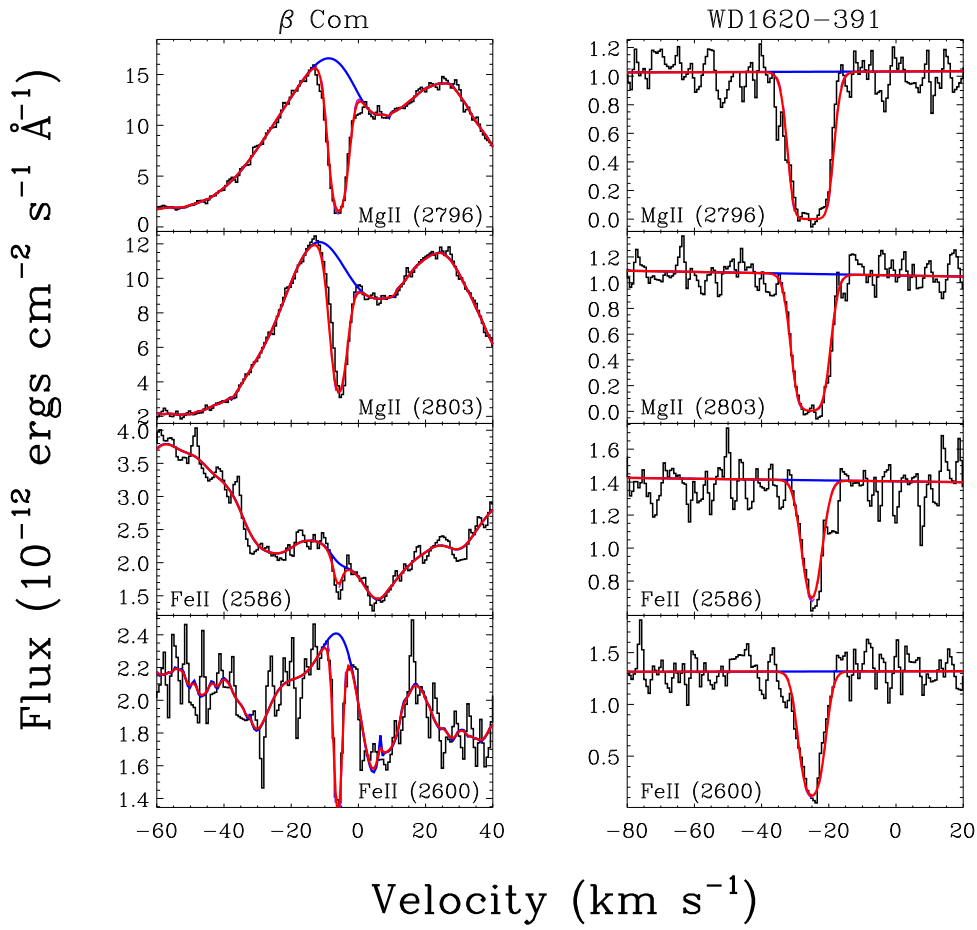


Figure 3.4: See caption of Figure 3.3.

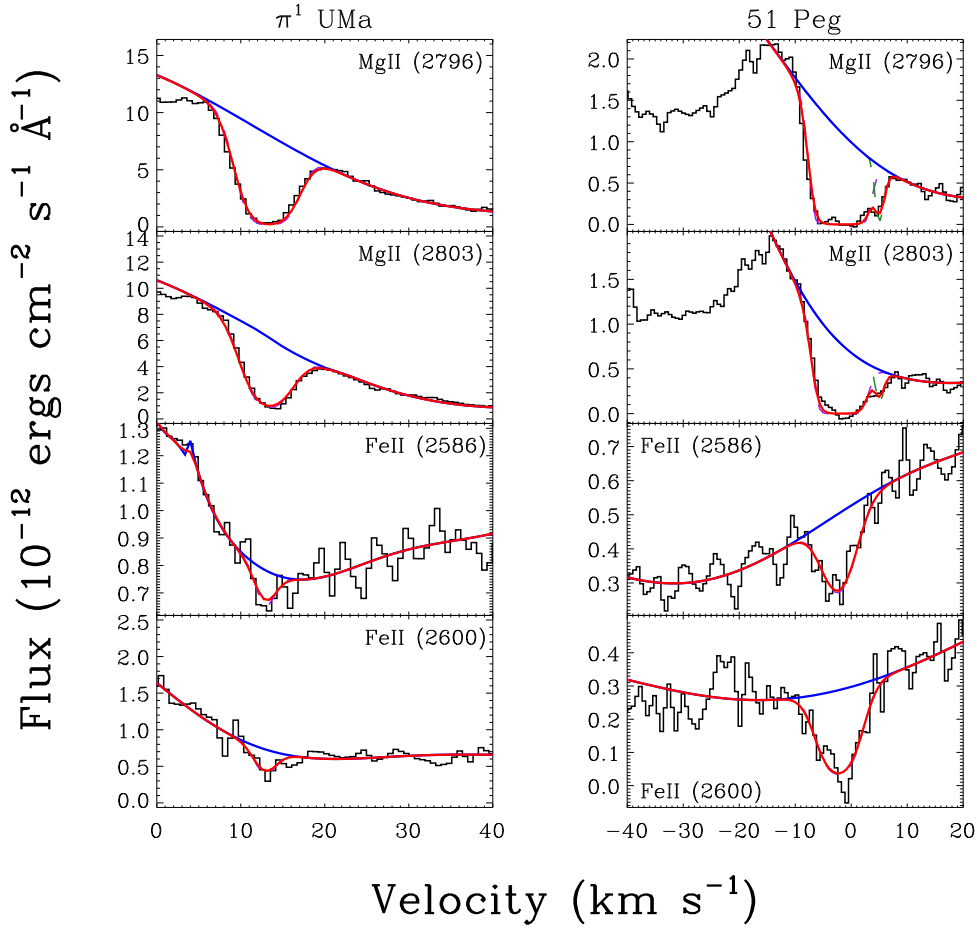


Figure 3.5: See caption of Figure 3.3.

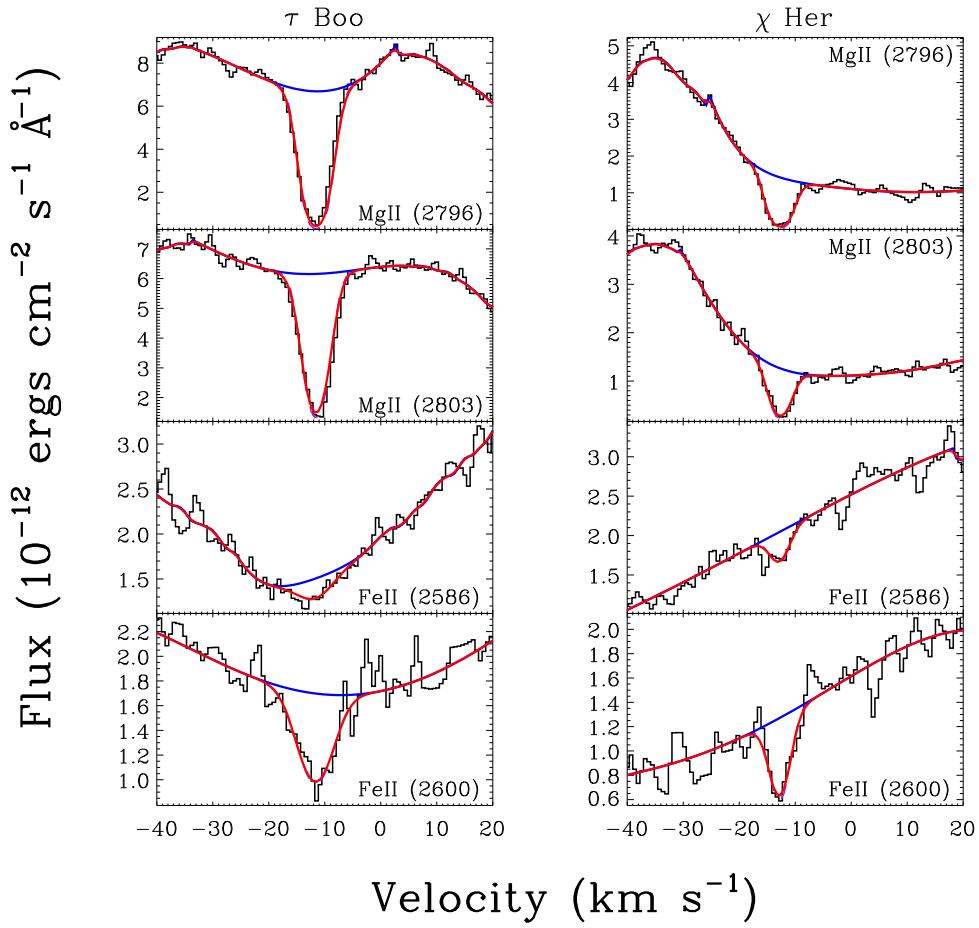


Figure 3.6: See caption of Figure 3.3.

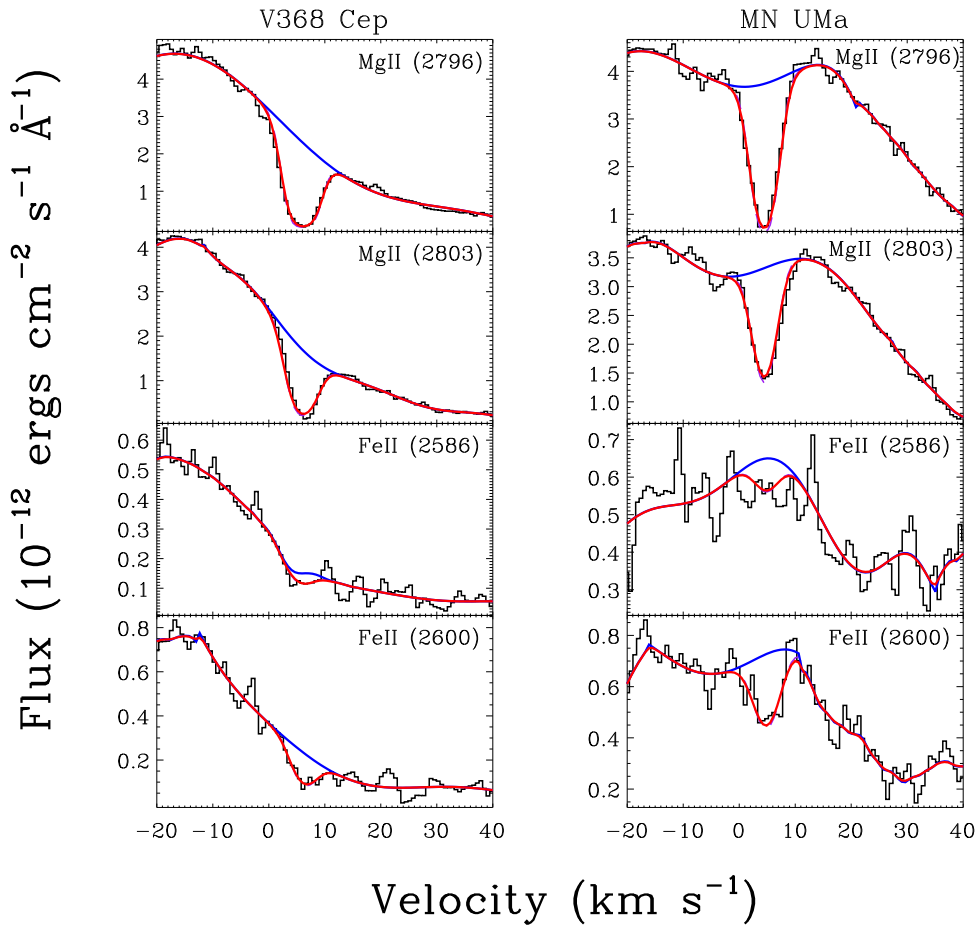


Figure 3.7: See caption of Figure 3.3.

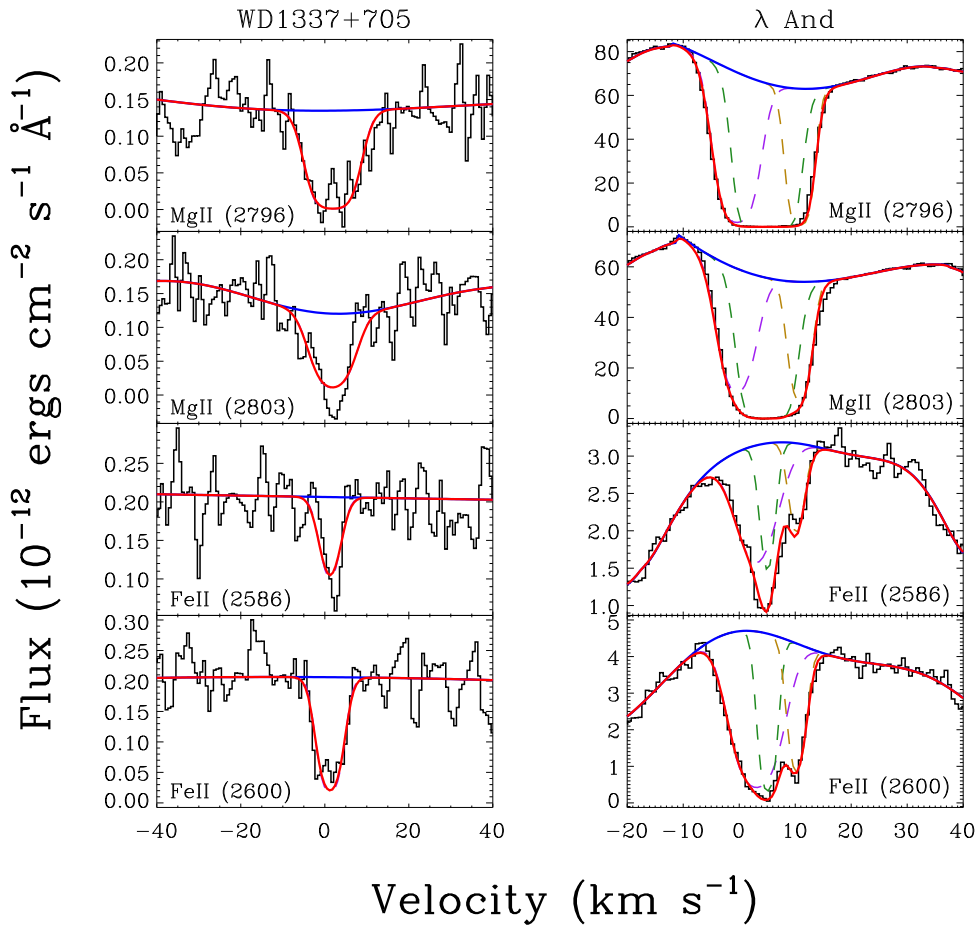


Figure 3.8: See caption of Figure 3.3.

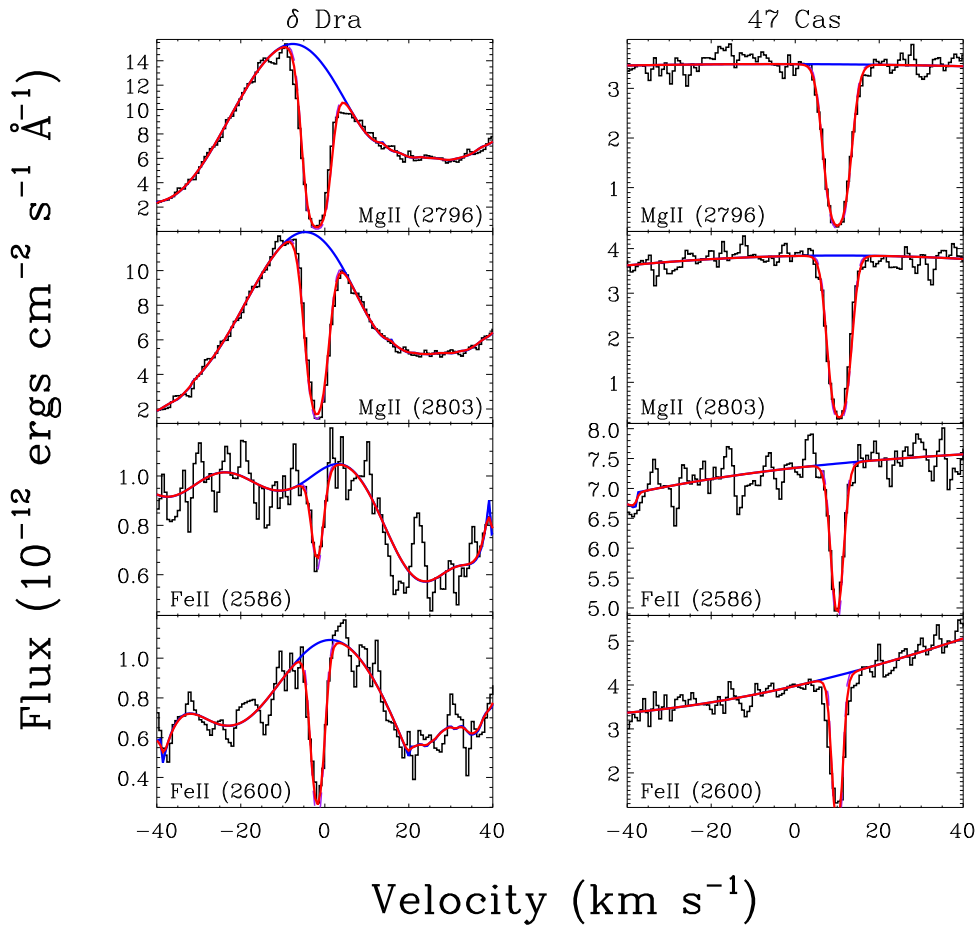
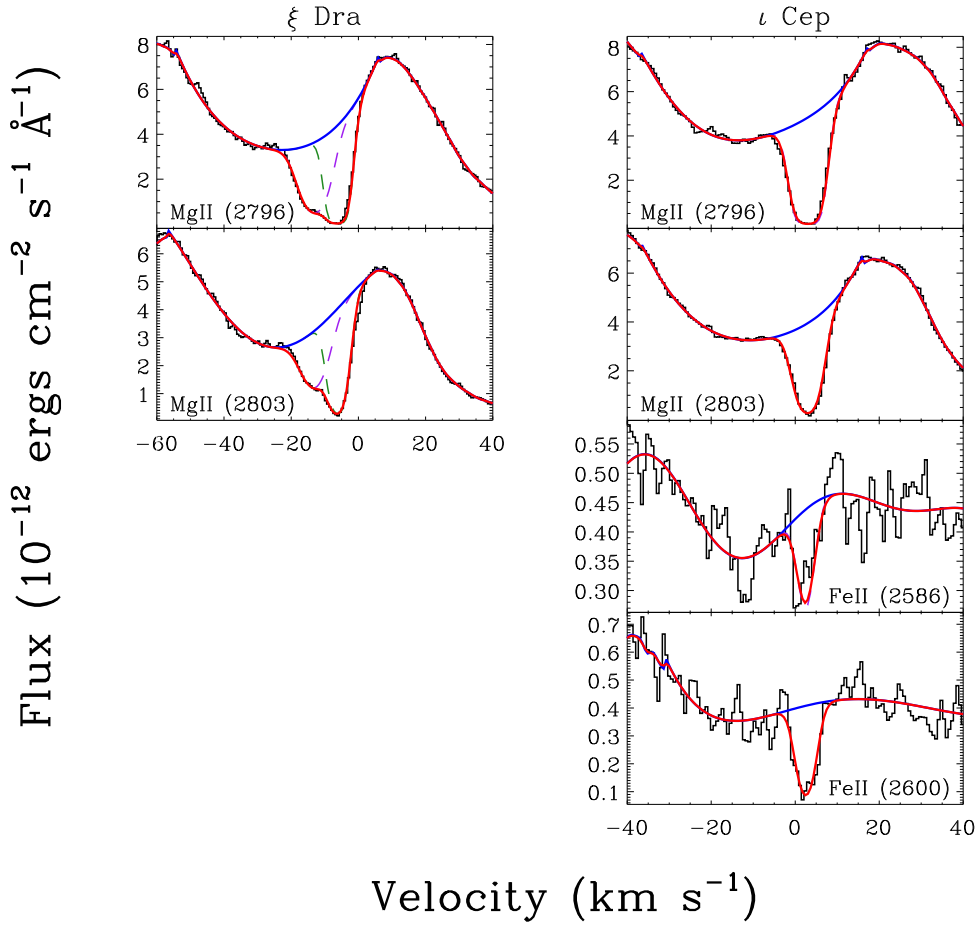


Figure 3.9: See caption of Figure 3.3.



**Figure 3.10:** See caption of Figure 3.3. No ISM features were detectable in FeII for  $\xi$  Dra.

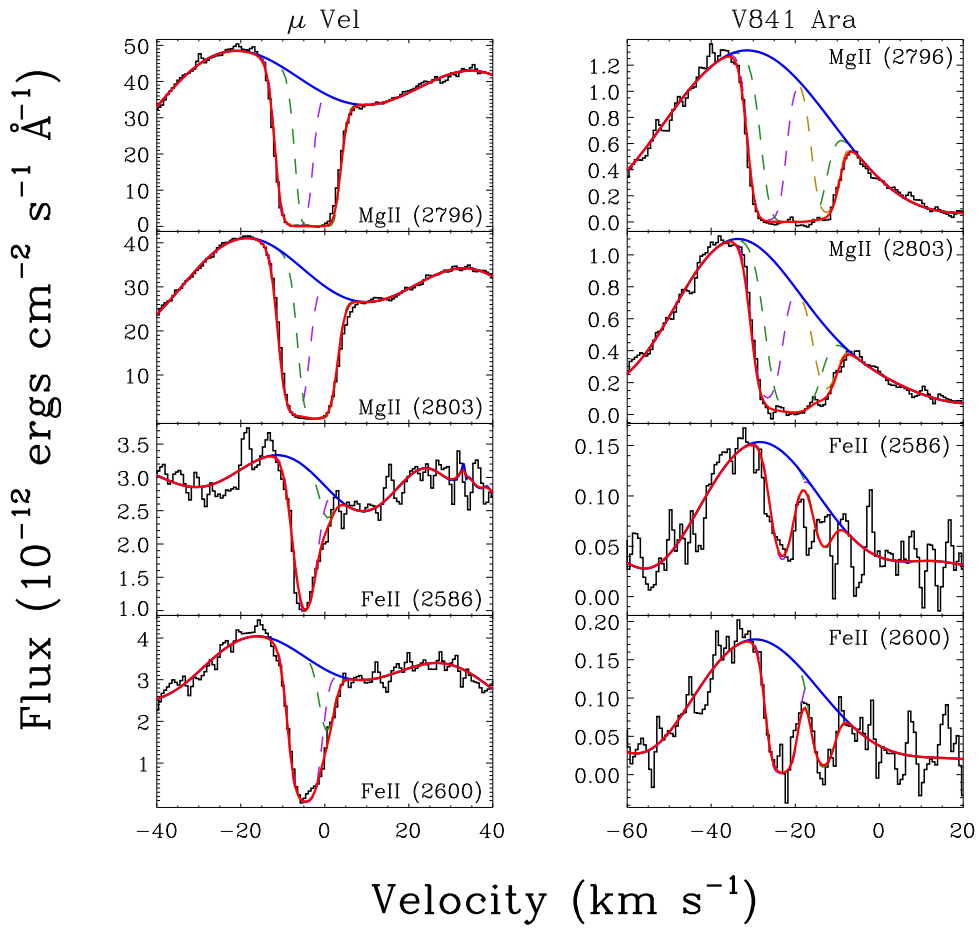


Figure 3.11: See caption of Figure 3.3.

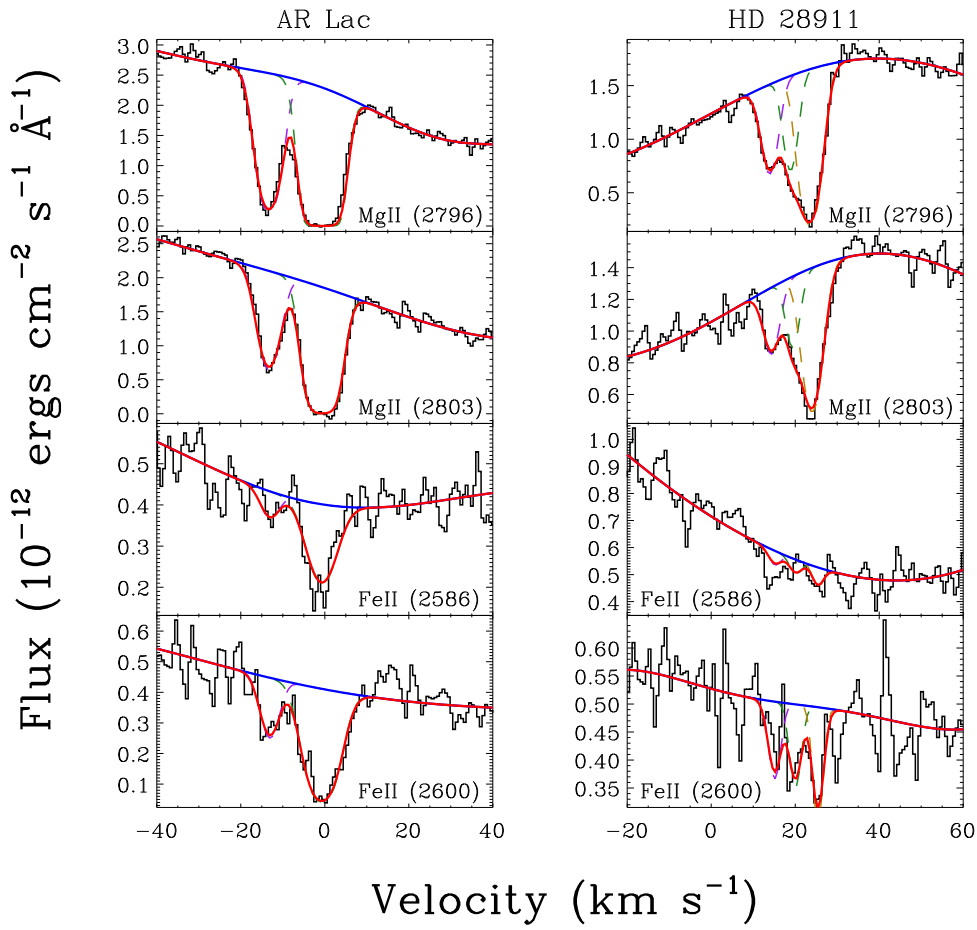


Figure 3.12: See caption of Figure 3.3.

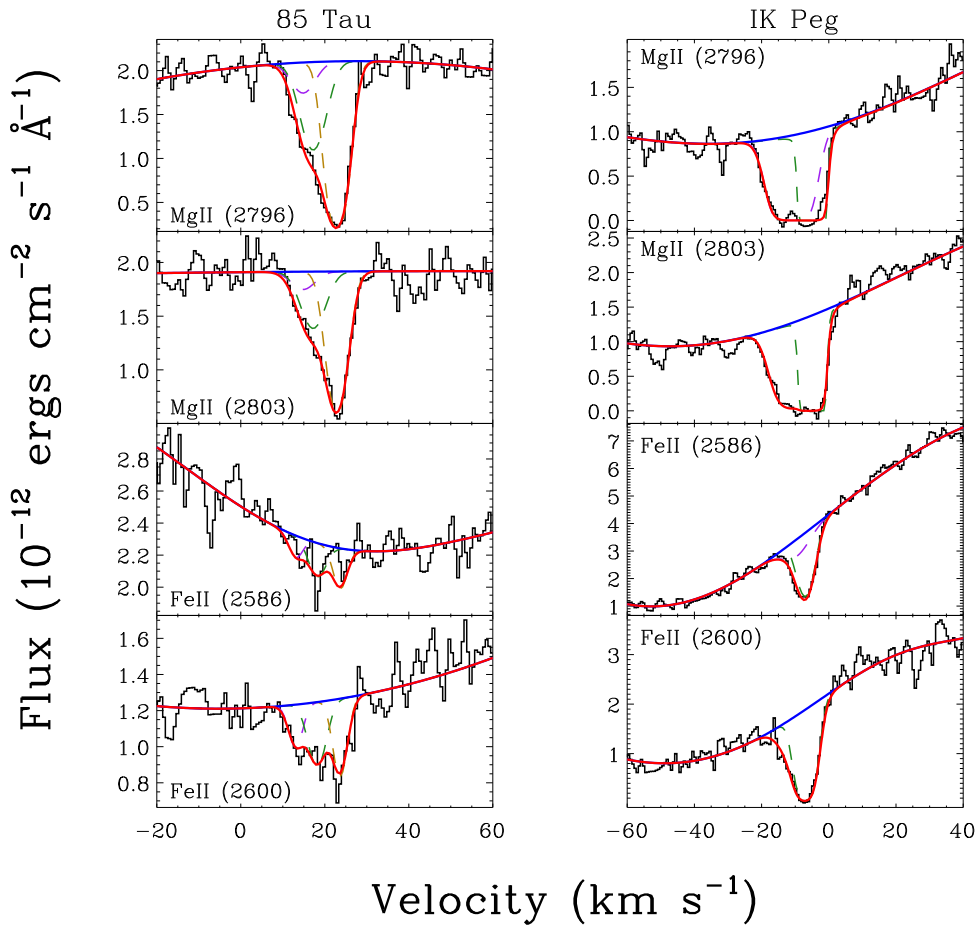


Figure 3.13: See caption of Figure 3.3.

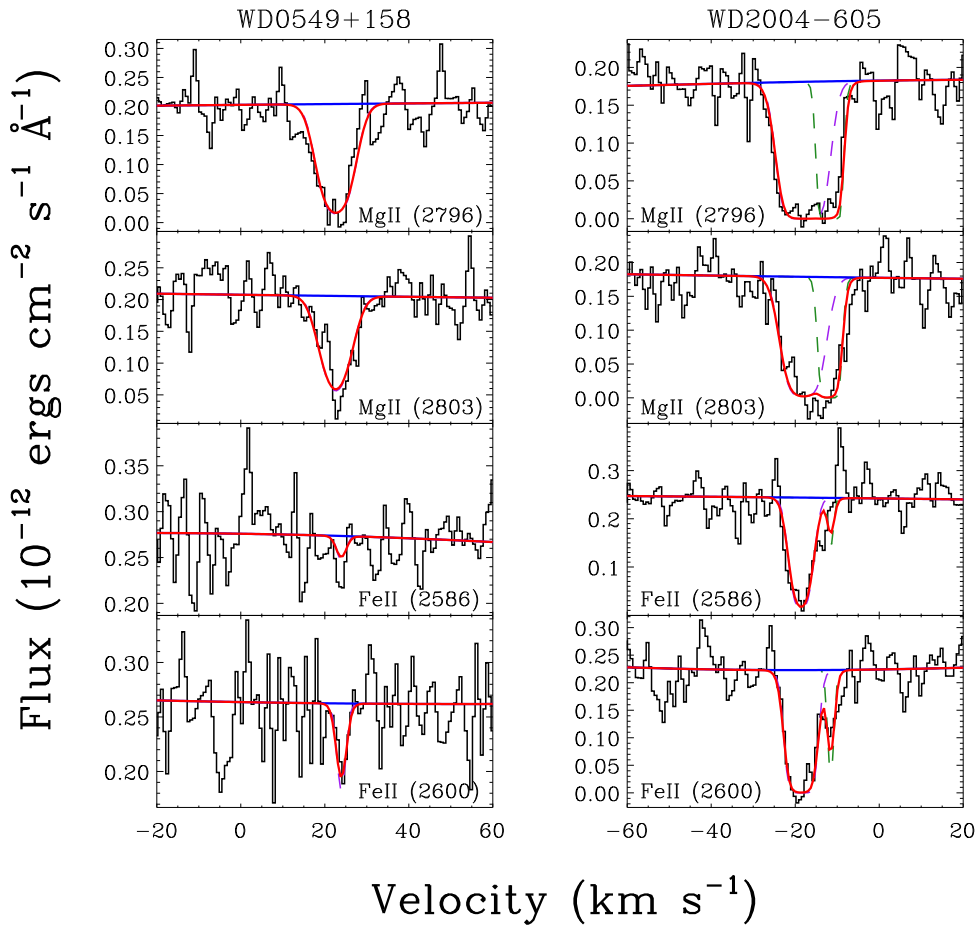


Figure 3.14: See caption of Figure 3.3.

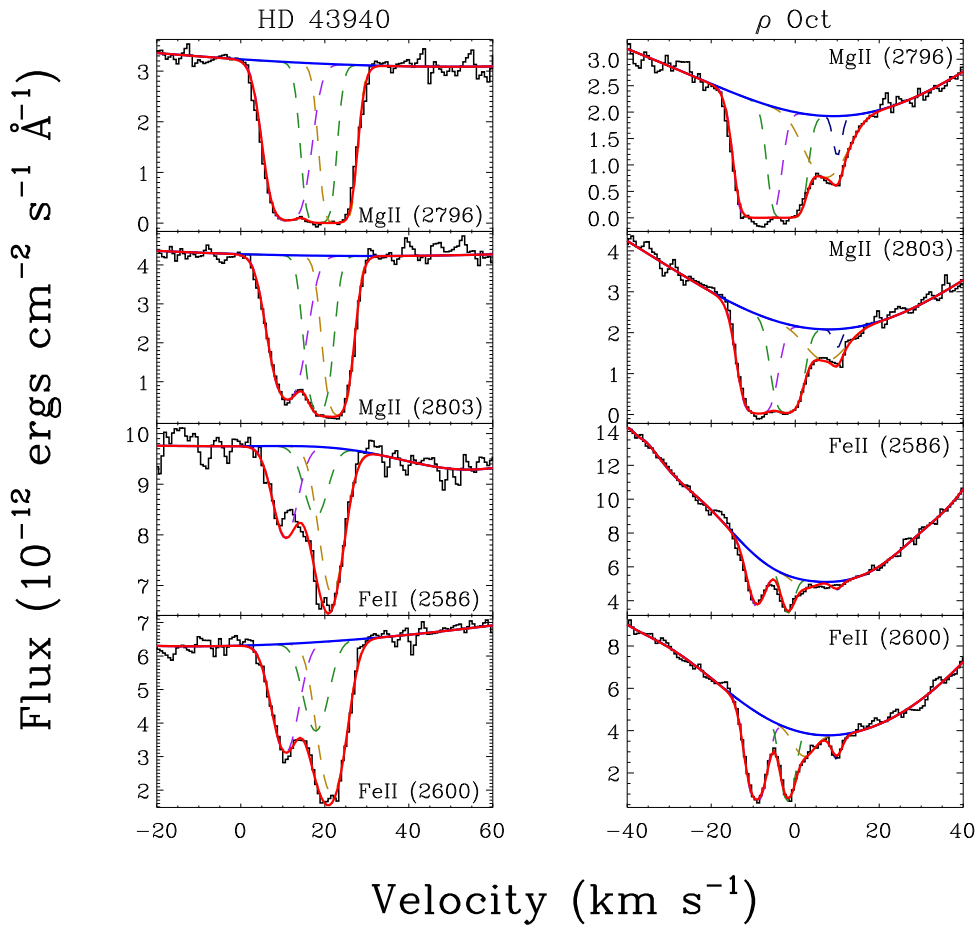


Figure 3.15: See caption of Figure 3.3.

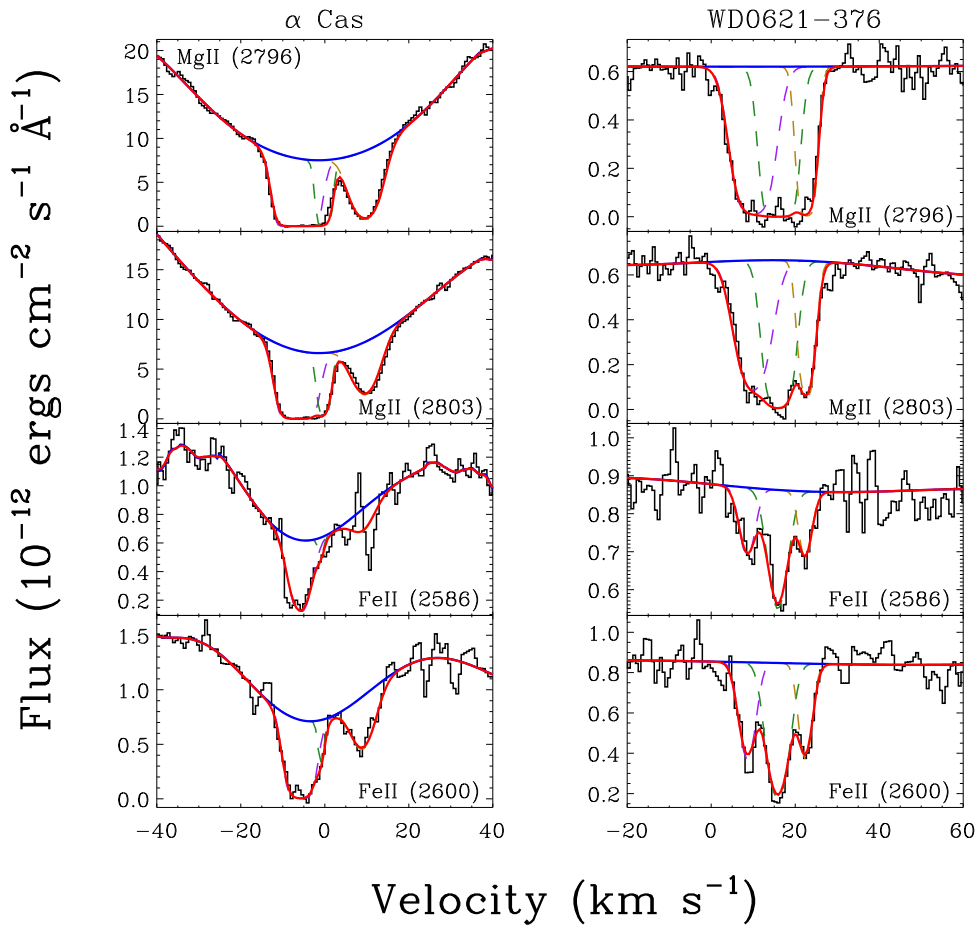


Figure 3.16: See caption of Figure 3.3.

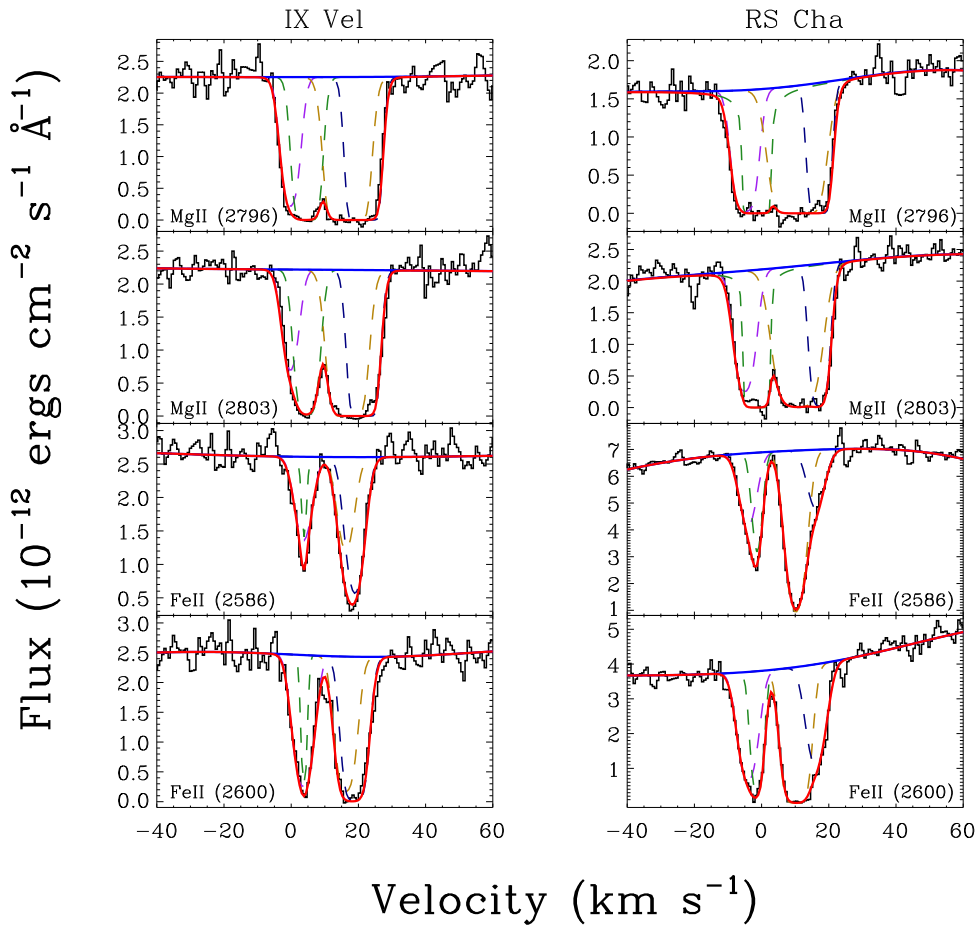
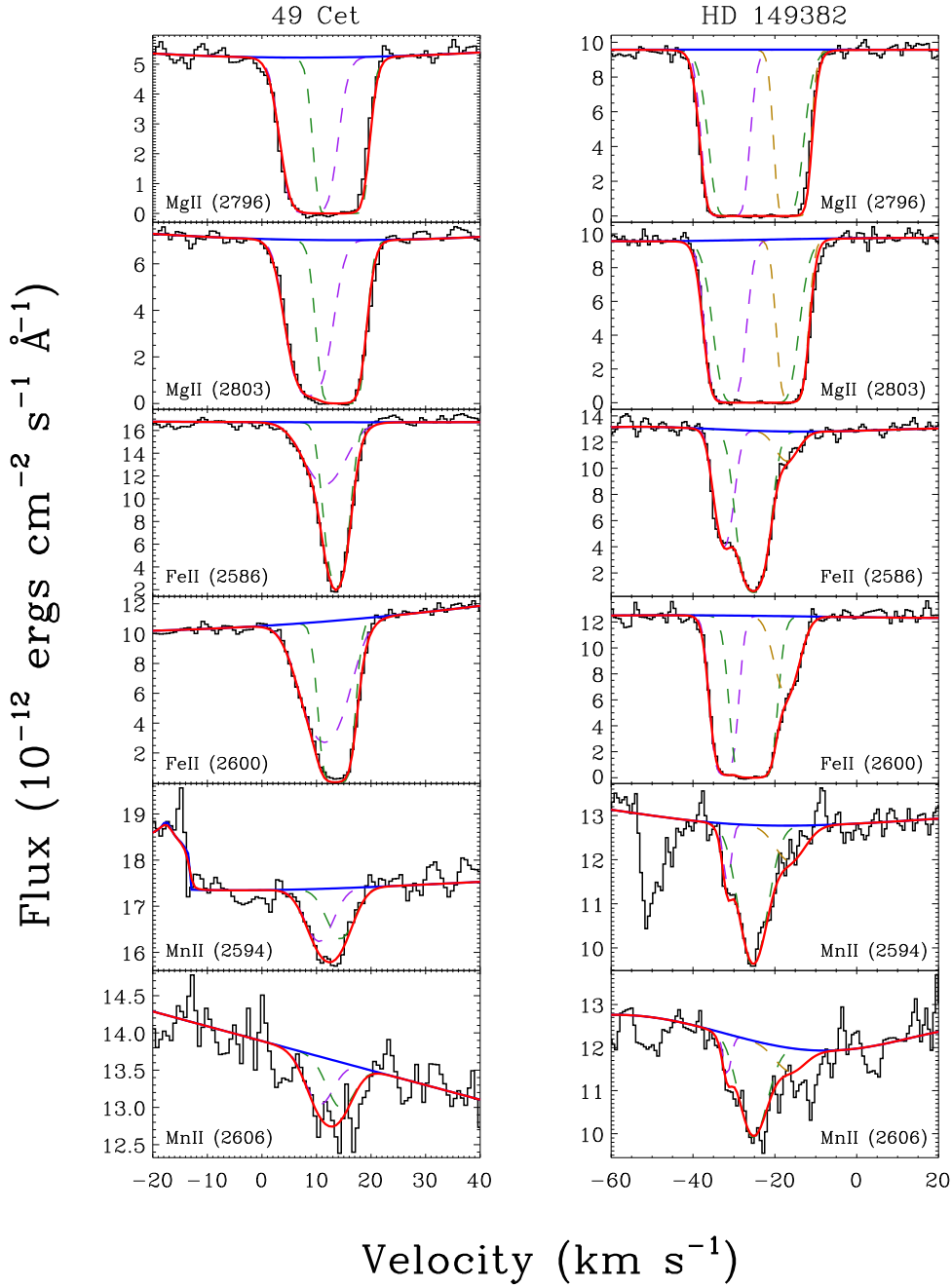


Figure 3.17: See caption of Figure 3.3.



**Figure 3.18:** See caption of Figure 3.3. Also includes MnII fits.

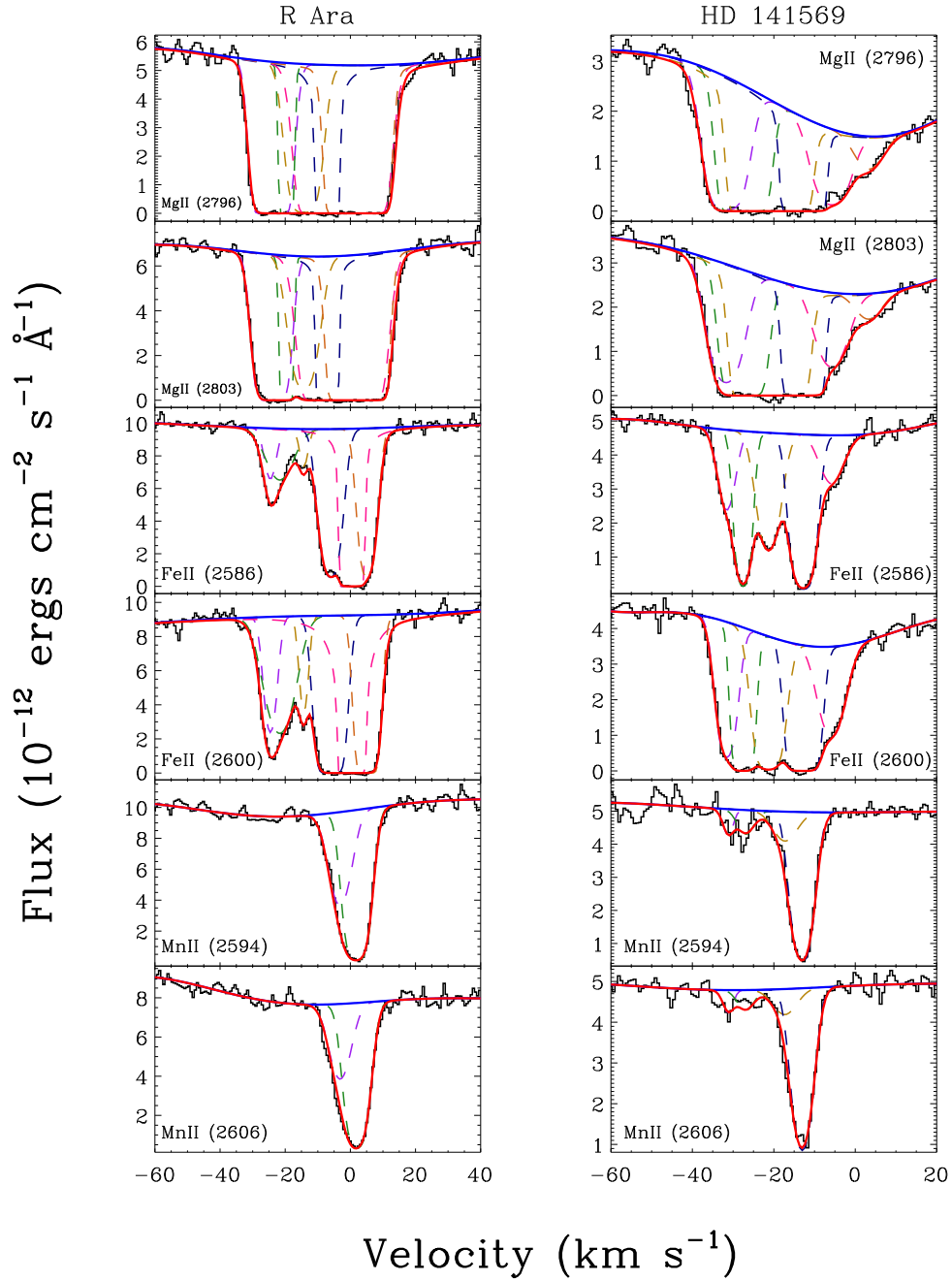


Figure 3.19: See caption of Figure 3.18.

## 3.6 Results

Many of the longest sight lines in this sample had both saturated and blended components. Under the assumption that MgII, FeII, and MnII are well mixed within a cloud, the velocities of unsaturated lines were used as a constraint on the spacing of the components in the saturated line. Such sight lines proved challenging to fit because they do not provide constraints on the Doppler parameters or column densities of the components. For example, six ISM components were detected towards HD 149730, a sight line 80.4 pc long (Figure 3.19). This would be impossible to determine using solely MgII which is completely saturated and blended. The velocities determined from the FeII and MnII fits were used to fix the spacing of the six components in the MgII line, while their absolute velocities, Doppler widths, and column densities were free parameters in the fit.

In numerous cases, the simultaneous fits highlight a systematic error in the radial velocity measurement. One of the more egregious examples is  $\beta$  Com (Figure 3.4). To test if the issue was my continuum placement, I took the difference between my simultaneous fit and the data and subtracted it from my original continuum. I then used this array as my new continuum. It corrected the issue, but I concluded that the sharp undulations necessary to do so were physically unrealistic. A second hypothesis was that the two lines fell on different orders of the echelle spectrograph and were imprecisely spliced together during the data reduction process. I fit the MgII *h* and *k* lines from the same order and different orders and compared them both to the fully-reduced data. The velocity discrepancy was smallest on the fully-reduced data, ruling out this hypothesis. As of this writing, the problem has not been resolved, but is likely an issue with the wavelength calibration either in the `calstis` or StarCAT reduction pipelines. Nevertheless,

the average discrepancy between the velocities is only  $\sim 0.2 \text{ km s}^{-1}$  ( $< 10\%$  of the resolution element) and is accounted for in the uncertainties.

### 3.7 Final Fit Parameters

The following tables list the final parameters of the fitting procedure. These parameters include the velocities ( $v$ ), Doppler parameters ( $b$ ), and log column densities ( $\log N$ ). Each value is a weighted mean using the parameter values in the individual and simultaneous fits. Components seen in MgII but not in FeII or MnII have upper limits listed in the column density columns.

Table 3.1. Fit Parameters for MgII LISM Components within 100 pc

HD No.	Other Name	Component No.	$v$ (km s <sup>-1</sup> )	$b$ (km s <sup>-1</sup> )	$\log N_{\text{MgII}}$ $\log(\text{cm}^{-2})$
209100	$\epsilon$ Ind	1	-10.83 ± 0.36	3.099 ± 0.011	12.84 ± 0.041
115617	61 Vir	1	-14.73 ± 0.42	2.69 ± 0.11	12.4710 ± 0.0089
114710	$\beta$ Com	1	-5.86 ± 0.34	2.84 ± 0.23	12.453 ± 0.027
	WD1620-391	1	-25.42 ± 0.37	4.29 ± 0.52	13.11 ± 0.18
72905	$\pi^1$ UMa	1	13.32 ± 0.28	3.070 ± 0.066	12.671 ± 0.033
217014	51 Peg	1	-1.94 ± 0.31	3.09 ± 0.14	13.38 ± 0.11
		2	5.01 ± 0.15	0.93 ± 0.37	11.936 ± 0.025
120136	$\tau$ Boo	1	-11.61 ± 0.26	2.74 ± 0.13	12.51 ± 0.05
142373	$\chi$ Her	1	-12.69 ± 0.16	2.213 ± 0.046	12.465 ± 0.016
220140	V368 Cep	1	6.04 ± 0.23	2.76 ± 0.32	12.65 ± 0.02
97334	MN UMa	1	4.54 ± 0.19	2.636 ± 0.086	12.270 ± 0.024
	WD1337+705	1	1.83 ± 0.39	4.7 ± 1.2	12.955 ± 0.077
222107	$\lambda$ And	1	0.14 ± 0.76	3.62 ± 0.28	12.75 ± 0.13
		2	4.975 ± 0.057	3.40 ± 1.27	13.17 ± 0.22
		3	10.17 ± 0.85	2.58 ± 0.51	12.66 ± 0.18
180711	$\delta$ Dra	1	-1.90 ± 0.28	2.715 ± 0.073	12.65 ± 0.021
12230	47 Cas	1	10.27 ± 0.17	2.49 ± 0.26	12.62 ± 0.13
163588	$\xi$ Dra	1	-13.72 ± 0.81	4.57 ± 0.53	12.505 ± 0.087
		2	-6.27 ± 0.42	3.49 ± 0.27	12.852 ± 0.031
216228	$\iota$ Cep	1	3.06 ± 0.20	3.407 ± 0.055	12.880 ± 0.023
93497	$\mu$ Vel	1	-7.2 ± 1.3	3.08 ± 0.40	12.913 ± 0.090
		2	1.2 ± 1.7	3.33 ± 0.21	13.13 ± 0.13
149499	V841 Ara	1	-25.90 ± 0.63	3.402 ± 0.036	12.87 ± 0.24
		2	-19.56 ± 0.91	2.5 ± 2.3	13.22 ± 0.20
		3	-13.32 ± 0.68	3.13 ± 0.31	12.58 ± 0.16
210334	AR Lac	1	-13.32 ± 0.34	3.19 ± 0.12	12.478 ± 0.013
		2	-0.63 ± 0.33	3.82 ± 0.43	13.08 ± 0.15
28911	HIP21267	1	14.30 ± 0.20	2.47 ± 0.41	11.894 ± 0.055
		2	20.3 ± 2.2	2.4 ± 1.6	11.84 ± 0.31
		3	23.83 ± 0.45	3.07 ± 0.87	12.17 ± 0.33
28677	85 Tau	1	13.81 ± 0.77	2.7 ± 1.2	11.42 ± 0.19
		2	18.6 ± 1.1	3.42 ± 0.81	12.094 ± 0.096
		3	23.26 ± 0.39	2.91 ± 0.32	12.409 ± 0.056
204188	IK Peg	1	-12.2 ± 1.7	5.22 ± 0.92	12.92 ± 0.24
		2	-5.33 ± 0.64	2.51 ± 0.84	13.12 ± 0.56
	WD0549+158	1	22.58 ± 0.81	4.09 ± 0.21	12.6313 ± 0.0056
9672	49 Cet	1	9.0 ± 1.3	3.88 ± 0.51	12.97 ± 0.11
		2	14.4 ± 1.1	2.98 ± 0.42	13.36 ± 0.10
	WD2004-605	1	-17.90 ± 1.71	3.89 ± 0.31	13.17 ± 0.19
		2	-11.00 ± 0.44	2.15 ± 1.4	12.89 ± 0.24
43940	HR2265	1	10.19 ± 0.15 <sup>a</sup>	4.14 ± 0.26	12.654 ± 0.053
		2	15.16	6.22 ± 0.59	12.695 ± 0.040
		3	18.91	2.93 ± 0.66	12.63 ± 0.11
		4	22.51	3.53 ± 0.20	12.935 ± 0.050
137333	$\rho$ Oct	1	-8.82 ± 0.59	3.691 ± 0.063	13.161 ± 0.055
		2	-1.9 ± 1.0	2.91 ± 0.47	12.992 ± 0.095
		3	3.2 ± 3.4	4.4 ± 1.3	12.330 ± 0.050
		4	9.61 ± 0.60	3.3 ± 1.3	11.68 ± 0.53
3712	$\alpha$ Cas	1	-6.75 ± 0.45 <sup>a</sup>	3.57 ± 0.16	13.29 ± 0.10
		2	-2.46	2.83 ± 0.22	12.91 ± 0.24
		3	9.74 ± 0.50	3.88 ± 0.073	12.5526 ± 0.0024
149382	HIP81145	1	-32.02 ± 0.55 <sup>a</sup>	3.681 ± 0.089	13.211 ± 0.090
		2	-24.57	4.9 ± 1.3	13.92 ± 0.26
		3	-15.70	2.89 ± 0.23	13.059 ± 0.083
	WD0621-376	1	10.31 ± 0.65	4.68 ± 0.40	12.81 ± 0.14
		2	16.22 ± 0.54	3.2 ± 1.6	13.11 ± 0.14
		3	22.2 ± 1.4	2.50 ± 0.81	12.667 ± 0.037
149730	R Ara	1	-24.17 ± 0.59 <sup>a</sup>	4.3 ± 0.34	13.754 ± 0.013
		2	-19.59	1.29 ± 0.48	13.18 ± 0.10
		3	-14.23	3.5 ± 2.3	13.03 ± 0.16
		4	-7.05	4.1 ± 2.4	14.16 ± 0.15
		5	-2.39	6.4 ± 1.9	14.523 ± 0.060
	IX Vel	1	1.2 ± 1.9	3.22 ± 0.52	12.69 ± 0.31
		2	4.91 ± 0.37	2.72 ± 0.39	12.88 ± 0.26
		3	16.44 ± 0.32	3.91 ± 0.11	13.56 ± 0.21
		4	20.80 ± 0.73	3.49 ± 0.64	13.30 ± 0.21
75747	RS Cha	1	-4.86 ± 0.14 <sup>a</sup>	3.31 ± 0.47	12.744 ± 0.018
		2	-1.37	2.12 ± 0.98	13.46 ± 0.61
		3	10.68	4.7 ± 1.6	13.40 ± 0.24
		4	17.27	2.78 ± 0.24	12.84 ± 0.15
141569	HIP77542	1	-31.24 ± 0.55 <sup>a</sup>	4.44 ± 0.41	13.06 ± 0.12
		2	-26.90	3.0 ± 1.2	13.25 ± 0.41
		3	-20.54	3.8 ± 1.2	13.62 ± 0.43
		4	-12.24	2.45 ± 0.12	13.60 ± 0.75
		5	-5.36	4.85 ± 0.20	12.535 ± 0.098
		6	2.84 ± 0.34	4.18 ± 0.98	11.974 ± 0.062

<sup>a</sup>This uncertainty value applies to all other component velocities with no uncertainty given. These components were varied with fixed spacing when fitting velocities. Spacing based on unsaturated FeII or MnII lines.

Table 3.2. Fit Parameters for FeII LISM Components within 100 pc

HD No.	Other Name	Component Number	$v$ (km s <sup>-1</sup> )	$b$ (km s <sup>-1</sup> )	$\log N_{\text{FeII}}$ log(cm <sup>-2</sup> )
209100	$\epsilon$ Ind	1	-11.343 ± 0.080	2.77 ± 0.63	12.616 ± 0.080
115617	61 Vir	1	-14.24 ± 0.52	1.20 ± 0.65	11.96 ± 0.10
114710	$\beta$ Com	1	-6.04 ± 0.19	1.37 ± 0.27	12.080 ± 0.049
	WD1620-391	1	-25.04 ± 0.42	3.625 ± 0.047	12.99 ± 0.030
72905	$\pi^1$ UMa	1	13.10 ± 0.16	1.24 ± 0.35	12.029 ± 0.023
217014	51 Peg	1	-2.21 ± 0.28	3.76 ± 0.16	12.942 ± 0.015
		2	...	...	<12.1
120136	$\tau$ Boo	1	-11.68 ± 0.36	4.08 ± 0.22	12.398 ± 0.026
142373	$\chi$ Her	1	-12.76 ± 0.43	2.20 ± 0.34	12.281 ± 0.046
220140	V368 Cep	1	6.27 ± 0.95	2.72 ± 0.30	12.494 ± 0.082
97334	MN UMa	1	4.94 ± 0.33	3.19 ± 0.93	12.222 ± 0.099
	WD1337+705	1	1.34 ± 0.54	2.99 ± 0.91	12.895 ± 0.029
222107	$\lambda$ And	1	1.1 ± 2.3	4.0 ± 1.2	12.42 ± 0.35
		2	4.52 ± 0.41	2.58 ± 0.80	12.92 ± 0.26
		3	10.28 ± 0.037	1.82 ± 0.22	12.533 ± 0.027
180711	$\delta$ Dra	1	-1.76 ± 0.12	1.75 ± 0.18	12.483 ± 0.014
12230	47 Cas	1	10.036 ± 0.030	1.931 ± 0.073	12.480 ± 0.016
163588	$\xi$ Dra	1, 2	...	...	<12.3
216228	$\iota$ Cep	1	2.56 ± 0.34	2.662 ± 0.038	12.684 ± 0.029
93497	$\mu$ Vel	1	-5.25 ± 0.65	2.78 ± 0.67	12.86 ± 0.22
		2	-1.3 ± 2.1	2.83 ± 0.92	12.22 ± 0.40
149499	V841 Ara	1	-23.18 ± 0.27	3.03 ± 0.49	13.192 ± 0.092
		2	...	...	<12.6
		3	-13.3 ± 1.3	2.20 ± 0.53	12.83 ± 0.18
210334	AR Lac	1	-13.12 ± 0.46	2.65 ± 1.021	12.25 ± 0.060
		2	-0.77 ± 0.37	4.42 ± 0.86	13.040 ± 0.017
28911	HIP21267	1	14.35 ± 0.81	1.60 ± 0.76	11.69 ± 0.13
		2	18.9 ± 1.6	1.91 ± 0.85	11.850 ± 0.088
		3	25.21 ± 0.38	1.77 ± 0.64	11.992 ± 0.095
28677	85 Tau	1	14.64 ± 0.88	2.0 ± 1.3	11.77 ± 0.22
		2	18.59 ± 0.41	1.16 ± 0.72	11.85 ± 0.17
		3	23.43 ± 0.64	1.97 ± 1.22	11.82 ± 0.38
204188	IK Peg	1	-10.7 ± 2.0	3.5 ± 1.9	12.26 ± 0.32
		2	-6.97 ± 0.24	3.26 ± 0.12	13.098 ± 0.026
	WD0549+158	1	23.83 ± 0.52	1.438 ± 0.079	11.76 ± 0.13
9672	49 Cet	1	11.0 ± 1.6	4.74 ± 0.65	12.69 ± 0.22
		2	13.65 ± 0.15	2.50 ± 0.28	13.267 ± 0.074
	WD2004-605	1	-18.75 ± 0.29	2.50 ± 0.32	13.425 ± 0.040
		2	-12.3 ± 1.6	1.9 ± 0.85	12.27 ± 0.12
43940	HR2265	1	10.07 ± 0.81	3.68 ± 0.43	12.37 ± 0.11
		2	15.03 ± 0.55	3.3 ± 1.1	12.27 ± 0.17
		3	18.79 ± 0.092	2.016 ± 0.053	12.213 ± 0.079
		4	22.38 ± 0.14	3.37 ± 0.23	12.651 ± 0.032
137333	$\rho$ Oct	1	-9.27 ± 0.15	2.58 ± 0.18	12.772 ± 0.013
		2	-1.80 ± 0.22	1.87 ± 0.40	12.52 ± 0.10
		3	1.2 ± 1.2	2.7 ± 1.8	11.91 ± 0.27
		4	10.0 ± 1.7	1.4 ± 1.9	11.78 ± 0.12
3712	$\alpha$ Cas	1	-6.05 ± 0.59	2.97 ± 0.42	13.231 ± 0.095
		2	-1.8 ± 1.7	2.1 ± 1.5	11.83 ± 0.66
		3	8.95 ± 0.22 <sup>a</sup>	3.47 ± 0.16 <sup>a</sup>	12.435 ± 0.016 <sup>a</sup>
149382	HIP81145	1	-32.73 ± 0.35	2.70 ± 0.14	13.049 ± 0.042
		2	-25.28 ± 0.31	3.89 ± 0.38	13.66 ± 0.013
		3	-16.40 ± 1.68	3.8 ± 1.2	12.25 ± 0.19
	WD0621-376	1	8.76 ± 0.35	2.26 ± 0.76	12.39 ± 0.046
		2	15.93 ± 0.33	2.81 ± 0.48	12.733 ± 0.049
		3	22.41 ± 0.12	2.02 ± 0.21	12.27 ± 0.030
149730	R Ara	1	-24.15 ± 0.63	3.37 ± 0.58	12.877 ± 0.037
		2	-19.3 ± 1.8	2.5 ± 2.1	12.326 ± 0.095
		3	-14.28 ± 0.57	2.5 ± 1.6	12.477 ± 0.059
		4	-7.02 ± 0.98	3.14 ± 0.65	13.409 ± 0.054
		5	-0.5 ± 1.4	3.1 ± 1.3	14.25 ± 0.27
		6	5.22 ± 0.67	3.3 ± 1.2	13.24 ± 0.12
	IX Vel	1	3.63 ± 0.20	3.33 ± 0.18	12.866 ± 0.067
		2	4.06 ± 0.18	1.20 ± 0.23	12.49 ± 0.13
		3	16.1 ± 1.3	3.3 ± 1.1	12.96 ± 0.11
		4	18.26 ± 0.91	3.04 ± 0.32	13.09 ± 0.17
75747	RS Cha	1	-5.32 ± 1.22	2.88 ± 0.95	12.31 ± 0.30
		2	-1.84 ± 0.41	2.40 ± 0.35	12.89 ± 0.12
		3	10.22 ± 0.39	3.39 ± 0.15	13.40 ± 0.034
		4	16.8 ± 1.3	2.91 ± 1.1	12.54 ± 0.19
141569	HIP77542	1	-31.88 ± 0.28	2.56 ± 0.28	12.72 ± 0.13
		2	-27.55 ± 0.15	2.18 ± 0.93	13.443 ± 0.016
		3	-21.207 ± 0.065	3.11 ± 0.98	13.255 ± 0.010
		4	-12.89 ± 0.23	2.87 ± 0.53	13.681 ± 0.029
		5	-6.0 ± 1.1	4.11 ± 0.53	12.74 ± 0.12
		6	...	...	<11.7

<sup>a</sup>The third component of  $\alpha$  Cas could not be fit individually in the 2586 Å line. Therefore, all final parameters for this component are the weighted means of the parameters in the 2600 Å individual fit and the simultaneous fit.

Table 3.3. Fit Parameters for MnII LISM Components within 100 pc

HD No.	Other Name	Component Number	$v$ (km s <sup>-1</sup> )	$b$ (km s <sup>-1</sup> )	$\log N_{\text{MnII}}$ log(cm <sup>-2</sup> )
209100	$\epsilon$ Ind	...	...	...	<11.8
115617	61 Vir	...	...	...	<11.8
114710	$\beta$ Com	...	...	...	<11.6
	WD1620-391	...	...	...	<12.2
72905	$\pi^1$ UMa	...	...	...	<12.0
217014	51 Peg	...	...	...	<11.5
120136	$\tau$ Boo	...	...	...	<11.6
142373	$\chi$ Her	...	...	...	<11.5
220140	V368 Cep	...	...	...	<12.5
97334	MN UMa	...	...	...	<11.9
	WD1337+705	...	...	...	<12.3
222107	$\lambda$ And	...	...	...	<11.8
180711	$\delta$ Dra	...	...	...	<11.8
9672	49 Cet	1	10.47 $\pm$ 0.80	3.61 $\pm$ 0.66	11.345 $\pm$ 0.097
		2	14.42 $\pm$ 0.82	3.41 $\pm$ 0.72	11.32 $\pm$ 0.11
12230	47 Cas	...	...	...	<11.9
163588	$\xi$ Dra	...	...	...	<12.1
216228	$\iota$ Cep	...	...	...	<12.0
93497	$\mu$ Vel	...	...	...	<11.6
149499	V841 Ara	...	...	...	<12.7
210334	AR Lac	...	...	...	<12.0
28911	HIP21267	...	...	...	<11.9
28677	85 Tau	...	...	...	<11.5
204188	IK Peg	...	...	...	<11.5
	WD0549+158	...	...	...	<12.2
	WD2004-605	...	...	...	<12.2
43940	HR2265	...	...	...	<11.4
137333	$\rho$ Oct	...	...	...	<12.2
3712	$\alpha$ Cas	...	...	...	<11.8
149382	HIP81145	1	-31.28 $\pm$ 0.79	1.83 $\pm$ 0.82	11.27 $\pm$ 0.16
		2	-25.41 $\pm$ 0.91	3.9 $\pm$ 1.4	11.921 $\pm$ 0.076
		3	-14.3 $\pm$ 4.7	4.04 $\pm$ 0.84	11.639 $\pm$ 0.090
	WD0621-376	...	...	...	<12.0
149730	R Ara	1,2,3	...	...	<11.8
		4	-1.4 $\pm$ 1.7	4.82 $\pm$ 0.73	12.70 $\pm$ 0.14
		5	2.30 $\pm$ 0.38	3.48 $\pm$ 0.44	13.045 $\pm$ 0.049
	IX Vel	...	...	...	<11.9
75747	RS Cha	...	...	...	<11.5
141569	HIP77542	1	-31.23 $\pm$ 0.69	1.98 $\pm$ 0.71	11.59 $\pm$ 0.12
		2	-27.0 $\pm$ 1.4	1.68 $\pm$ 0.91	11.528 $\pm$ 0.081
		3	-17.2 $\pm$ 1.6	3.09 $\pm$ 0.98	11.84 $\pm$ 0.12
		4	-12.97 $\pm$ 0.48	2.93 $\pm$ 0.31	12.830 $\pm$ 0.012
		5,6	...	...	<11.5

# Chapter 4

## Analysis of the LISM Sample

With the fitting complete, we now have a sample of fit parameters that describe certain physical properties of the absorbing media along each line of sight. Between the 34 sight lines analyzed, 76 components were detected in MgII, 71 in FeII, and 12 in MnII. This chapter will explore what can be learned about the LISM as a whole from this sample. In parts of this analysis, MnII is excluded due to too few components detected.

Figure 4.1 shows the distribution of parameters for all observed ions. The parameters come from Tables 3.1, 3.2, and 3.3. Many of the outliers in the MgII distributions are the result of saturated and blended lines in which fits are only constrained by one side of the bluest and reddest components. These minimal constraints are reflected in the inflated uncertainties of these values. The more frequent occurrence of saturated and blended lines at larger distances demonstrates the unique advantages of studying the ISM locally.

### 4.1 The Velocity Distribution

The velocity distribution contains the projected velocities of absorbing material in the heliocentric rest frame. Although the clouds in the LISM have distinct motions, they move in the same general direction with similar velocities (Frisch et al. 2002). Therefore, most sight lines in this sample show clusters of compo-

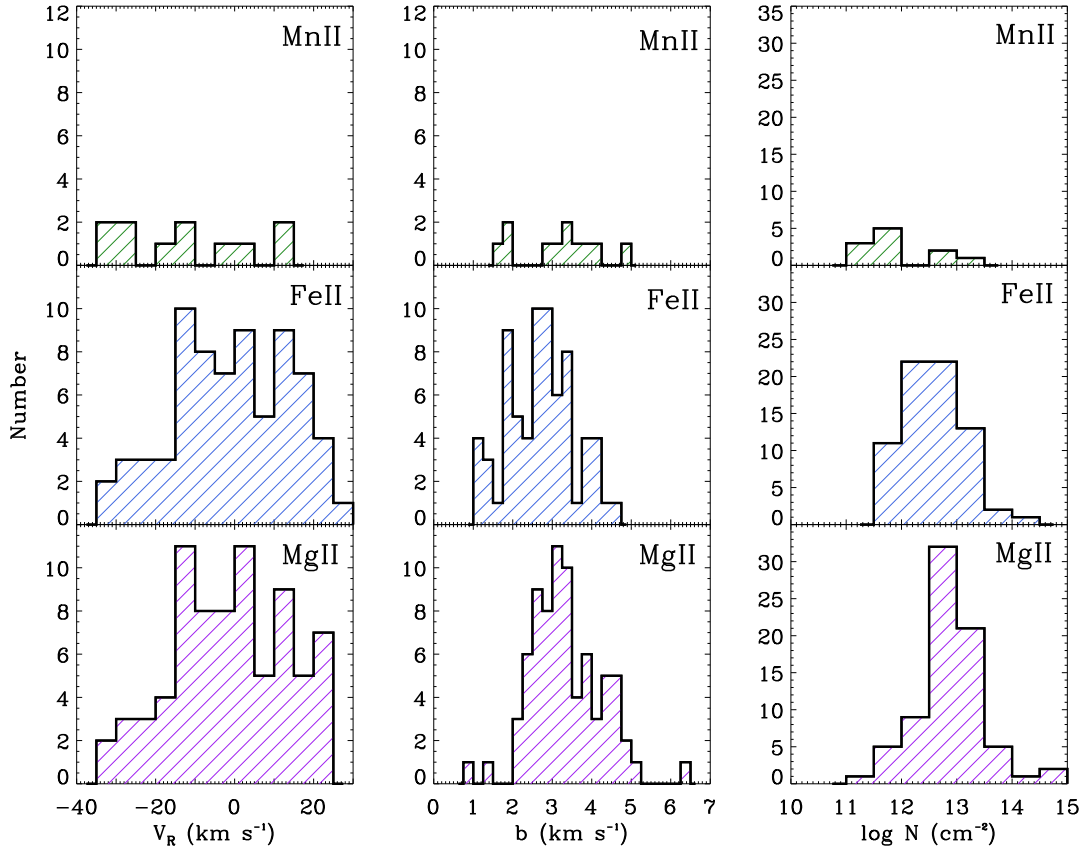


**Figure 4.1:** Distributions of radial velocity ( $V_R$ ), Doppler parameter ( $b$ ), and column density ( $N$ ) for the ions observed in this survey. The bin sizes are  $5 \text{ km s}^{-1}$ ,  $0.25 \text{ km s}^{-1}$ , and  $0.5 \log(\text{cm}^{-2})$  respectively.

nents in velocity space rather than isolated profiles. Only in the longest sight lines are a broader range of velocities detected. At long distances, clouds may be removed from the local bulk flow vector.

The velocities in the distribution range from  $-32$  to  $+25 \text{ km s}^{-1}$ , consistent with the bulk velocity of the warm LISM clouds:  $28.1 \pm 4.6 \text{ km s}^{-1}$  (Frisch et al. 2011). The general shape of the MgII and FeII distributions suggests that the ions are identifying the same clouds. If the pairing of components is reasonable, then the differences between  $v_{\text{MgII}}$  and  $v_{\text{FeII}}$  should produce a Gaussian distribution

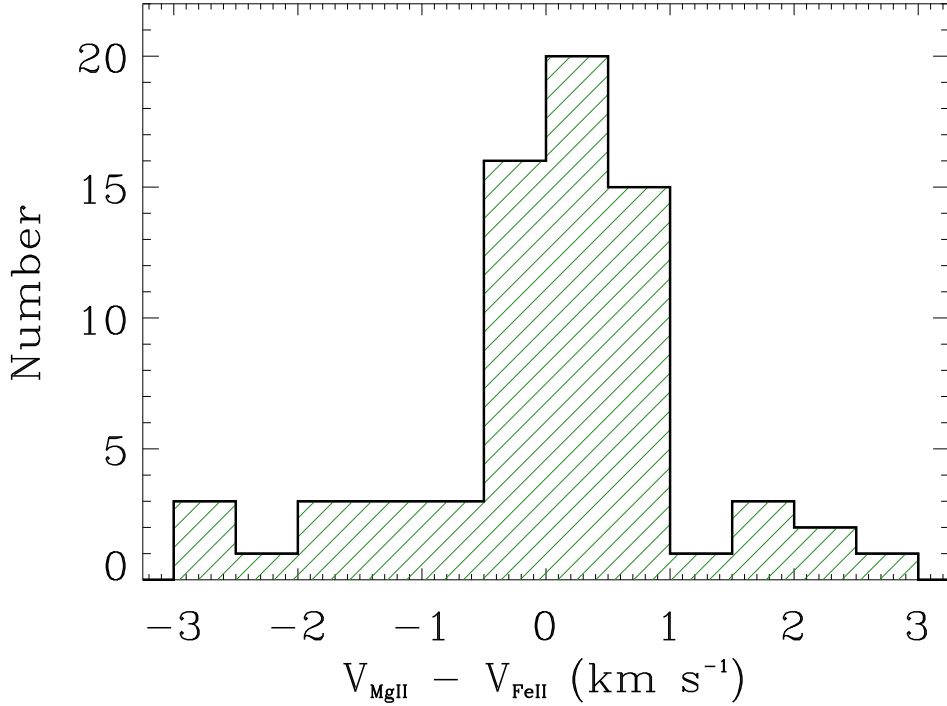


**Figure 4.2:** Distribution of differences between velocities of components measured with MgII and FeII. Their Gaussian-shaped distribution around  $\sim 0 \text{ km s}^{-1}$  indicates that these ion pairs belong to the same clouds.

peaked at  $0 \text{ km s}^{-1}$ . Figure 4.2 shows a distribution peaked slightly to the right of zero, suggesting a systematic error that caused the MgII velocities to generally be more positive than the FeII velocities. Still, the vast majority of velocities assumed to be from the same component are within  $1 \text{ km s}^{-1}$  ( $\sim 40\%$  of resolution element).

Table 4.1. Mean Values for Doppler Parameter and Log Column Density

Ion	$\langle b \rangle$ (km s <sup>-1</sup> )	$\sigma_b$ (km s <sup>-1</sup> )	$\langle \log N \rangle$ log(cm <sup>-2</sup> )	$\sigma_{\log N}$ log(cm <sup>-2</sup> )
MgII	3.36	0.90	12.89	0.58
FeII	2.72	0.84	12.61	0.54
MnII	3.16	0.99	11.91	0.65

## 4.2 The Doppler Parameter Distribution

The mean values for the Doppler parameters and log column densities are listed in Table 4.1. The following equation shows the dependence of the Doppler parameter ( $b$ ) on temperature ( $T$ ) and turbulent velocity ( $\xi$ ):

$$b^2 = \frac{2kT}{m} + \xi^2 = 0.016629 \frac{T}{A} + \xi^2, \quad (4.1)$$

where  $A$  is the ion's atomic weight in atomic mass units,  $k$  is the Boltzmann constant, and  $m$  is the ion's mass. MgII experiences greater Doppler broadening on average because it is a lighter ion and more susceptible to thermal broadening. Conversely, MnII and FeII should have roughly equivalent mean Doppler parameters because turbulence—the dominant broadening mechanism for heavier ions—is independent of atomic weight. The  $\langle b \rangle$  value of MnII is 0.4 km s<sup>-1</sup> greater than that of FeII, however. This discrepancy is due to the small number of MnII detections where the turbulence along a particular sight line greatly influences the mean. Redfield & Linsky (2002) report a  $\langle b(\text{FeII}) \rangle \sim 2.4$  km s<sup>-1</sup> with a  $\sigma_{\text{FeII}} \sim 1.0$  km s<sup>-1</sup> and a  $\langle b(\text{MgII}) \rangle \sim 3.1$  km s<sup>-1</sup> with  $\sigma_{\text{MgII}} \sim 0.8$  km s<sup>-1</sup>. Both means are 0.3 km s<sup>-1</sup> lower than my values, but the differences are not very significant.

Figure 4.3 compares the Doppler widths of MgII and FeII components. 71

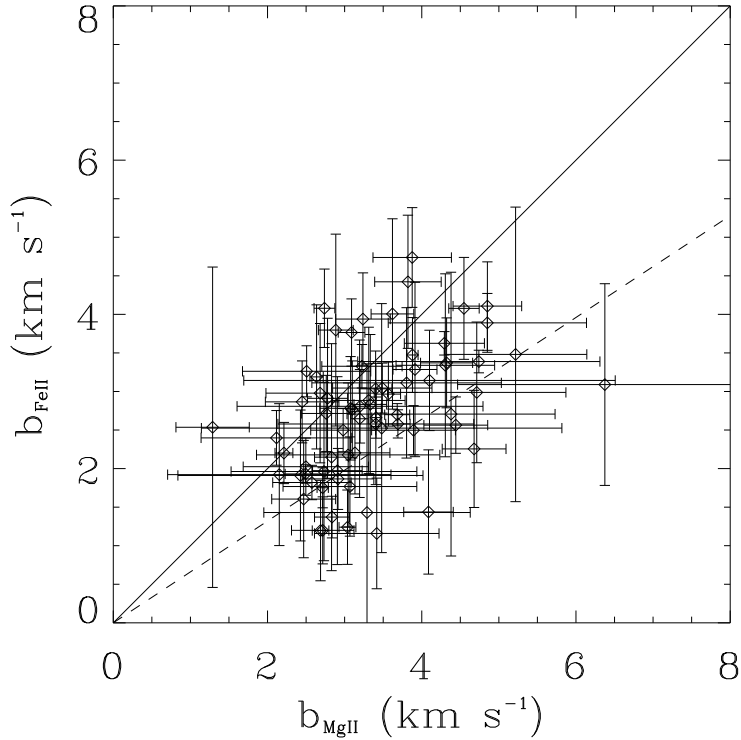


**Figure 4.3:** A plot comparing MgII and FeII Doppler parameters within the same clouds. The solid line demarcates broadening due solely to turbulence. The dashed line demarcates purely thermal broadening. One  $\sigma$  error bars are included. Should all the MgII and FeII pairings truly belong to the same clouds, we would expect each point to fall within the two lines. All but four fall within an error bar of this region, indicating the pairings are reasonable.

pairings were made based on their agreement in velocity. The solid line marks the ratio  $b_{\text{FeII}}/b_{\text{MgII}} = 1$ , which would only occur if there were no thermal broadening contributing to the line widths. If the broadening were entirely thermal, then one would expect a ratio of  $b_{\text{FeII}}/b_{\text{MgII}} = 0.66$ , determined by eliminating the  $\xi$  term from Equation 4.1. When both broadening mechanisms contribute to the

line width, the point should fall between the two lines. Indeed, 67 of the 71 components fall within this region or have at least one  $1\sigma$  error bar that does. Three of the remaining four have very weak FeII absorption that can result in an artificially broad or narrow fit. Alternatively, these unphysical ratios may highlight components in MgII and FeII that do not originate from the same cloud.

### 4.3 The Column Density Distribution

The column density distribution is also included in Figure 4.1, along with means and standard deviations for each ion listed in Table 4.1. MgII and FeII show similar column densities, but MnII is approximately an order of magnitude lower. While the MnII sample is small, this difference still holds true if one considers the average  $\log N_{\text{MnII}}$  upper limit of  $11.8 \log(\text{cm}^{-2})$ . The similarity in MgII and FeII column densities is attributable to two factors: both ions have comparable cosmic abundances and both are the dominant ionization species in the LISM (Slavin & Frisch 2008). The lower MnII column densities may be due in part to the solar abundance of Mn being approximately two orders of magnitude lower than Mg and Fe. The ionization fraction of MnII is not well-studied.

### 4.4 Number of Components Versus Distance

The sight lines in this sample contain anywhere from one to six components. As would be expected, the number of components correlates with the length of the sight line (Figure 4.4). This does not, however, provide a confident assessment of the distribution of clouds as a function of distance. The clouds may be densely clustered around the solar system or evenly distributed throughout the Local

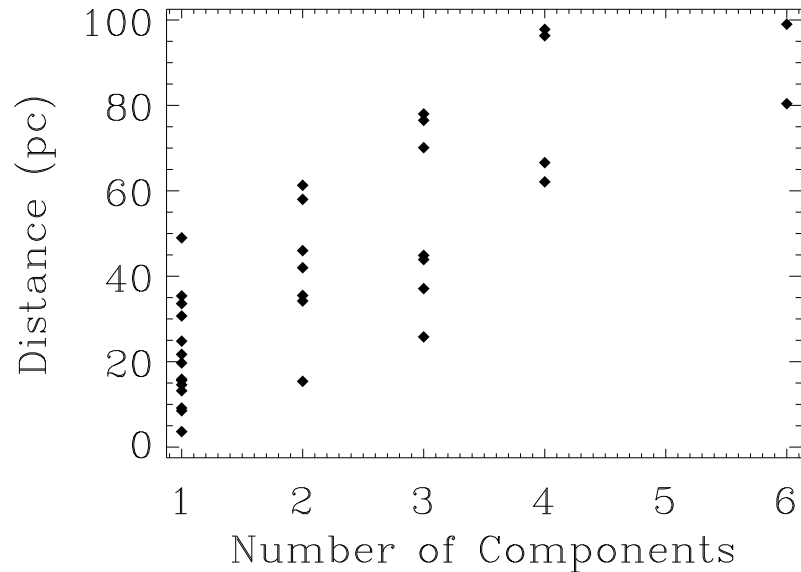


**Figure 4.4:** As the length of the sight line increases, the number of absorbers tends to increase as well. This trend suggests a prevalence of discrete clouds within the Local Bubble.

Bubble. To test these possibilities, Redfield & Linsky (2004a) examine sight lines in 10 pc distance bins to see how the average number of components per sight line changes with distance. The distance of each star provides an upper limit to the starting point of each cloud. A uniform distribution of clouds would show a steady increase in the average cloud number per 10 pc increment. Instead, their distribution remains flat after 30 pc, suggesting that LISM clouds are concentrated close to the solar system. Their sample, however, suffers from an under sampling of sight lines approaching 100 pc. In addition, the few distant sight lines happen to be located towards high galactic latitudes where they detect little LISM material.

In an effort to improve this measurement, I added my sample, which includes seven sight lines longer than 70 pc as well as many more shorter sight lines. The new distribution (Figure 4.5) shows a slight positive trend within the first 50

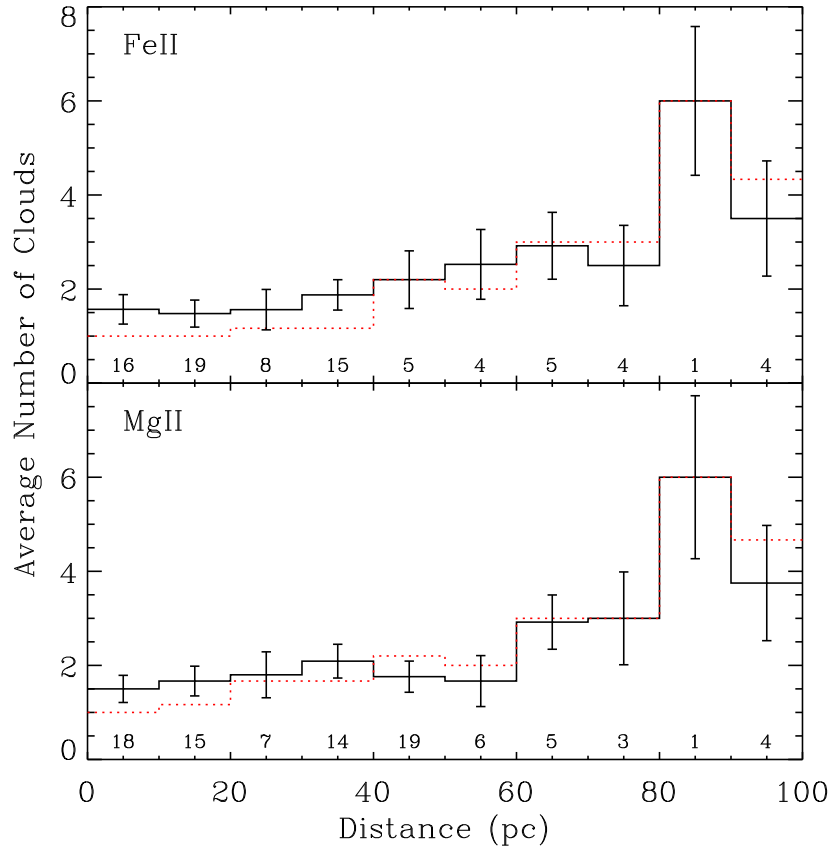


**Figure 4.5:** Distribution of the average number of components in 10 pc bins. Poisson counting errors are included. The solid black line shows the averages of the Redfield & Linsky (2004a) data set combined with this sample. The dotted line shows the distribution using only this sample. Centered at the bottom of each bin are the number of sight lines in each bin. Both distributions indicate that the average cloud number stays fairly constant out until 50–70 pc, supporting the conclusion by Redfield & Linsky (2004a) that most clouds in the Local Bubble being within 15 parsecs of the Sun. The rise is likely due to the onset of the Local Bubble edge in certain directions.

pc, but the Poisson error bars are such that this rise may be insignificant. This consistency in the average number of absorbers indicates that most clouds within 50 parsecs begin within 10 pc of the Sun. More measurements are needed to determine if the slight rise is real. Between 50 and 70 pc, there is a jump in the average number of absorbers. This may be related to the onset of the closest

---

edge the Local Bubble at  $\sim 55\text{--}60$  pc Lallement et al. (2003). The rise appears to continue out to 100 parsecs, but greater sampling of the LISM with long sight lines is needed to confirm this trend.

# Chapter 5

## Discussion

The addition of 34 sight lines to the sample of heavy ions observed in the LISM opens up many avenues for further research. These sight lines will provide independent tests of LISM cloud velocity vectors and unlock temperature and turbulence information. Oftentimes, serendipitous overlap with other areas of research results in unexpected directions of investigation. Included in this section are multiple examples of how this sample is used to address these other research questions. Two stars in the sample happen to have disk systems and may show gas absorption in the NUV. Other stars show the signature of astrospheres and their modeling would benefit from better knowledge of the foreground ISM velocity structure. Sight lines with small angular separations offer the opportunity to analyze the fine structure of the LISM and provide tighter constraints on cloud boundaries. Below, I present several applications of the new data set, some of which will be expanded in future work.

### 5.1 Comparison with Dynamical Model

In order to solve for a single velocity vector of an LISM cloud, one needs a correlation of velocities in a patch of sky. As of right now, 15 LISM clouds have been identified within 15 pc employing 81 NUV sight lines (Redfield & Linsky 2008). This new sample adds 34 NUV sight lines as long as 100 pc, dramatically

increasing the sample size and enabling the measurement of more cloud velocities with greater angular resolution.

Accompanying their paper, Redfield & Linsky (2008) provide an online “Kinematic Calculator”<sup>1</sup> that returns the projections of all 15 cloud velocity vectors towards any direction in the sky. It also lists any clouds predicted to be along the line of sight and within  $\sim 20^\circ$ . The  $\sim 20^\circ$  is a rough average estimate of the error in projected cloud boundaries. The first step in testing the model is to compare each component’s velocity to the radial velocities of the clouds predicted along the line of sight. If the difference between the observed and predicted velocities is within  $3\sigma$  of zero, the cloud is considered a match. If more than one component along a line of sight matches the prediction, the one that agrees best is chosen. The remaining components are then compared to the remaining predictions, including the nearby clouds.

When a component best matches a nearby cloud, it presents an opportunity to revise the cloud’s boundaries. The boundaries were originally constructed by drawing contours around sight lines that show spatial and kinematic similarities. The addition of more sight lines essentially increases the “resolution” of the cloud boundaries, and may even point to zones of dynamic interaction between clouds.

In the event that a component is incompatible with the velocities of all nearby clouds, it is likely the signature of an unidentified cloud. Before the cloud is identified, however, a correlation of velocities on the sky must be established. Occasionally, a component’s velocity agrees with the velocity of a cloud that is not near the direction of the sight line, but their large angular separation usually requires a contrived cloud shape to avoid other sight lines where no detection of the cloud is made.

---

<sup>1</sup><http://lism.wesleyan.edu/LISMdynamics.html>

Table 5.1. Comparison with Dynamical Model

HD No.	Other Name	Distance (pc)	Component Number	$v$ (km s <sup>-1</sup> )	Cloud	Alternative Explanation
209100	$\epsilon$ Ind	3.63	1	$-10.83 \pm 0.35$	LIC	
115617	61 Vir	8.53	1	$-14.73 \pm 0.42$	NGP	
114710	$\beta$ Com	9.15	1	$-6.00 \pm 0.17$	NGP	
	WD1620-391	13.2	1	$-25.25 \pm 0.28$	G	
72905	$\pi^1$ UMa	14.6	1	$13.29 \pm 0.24$	LIC	
217014	51 Peg	15.4	1	$-1.94 \pm 0.31$	Eri	
			2	$5.01 \pm 0.55$	Hyades	
120136	$\tau$ Boo	15.6	1	$-11.64 \pm 0.21$	NGP	
142373	$\chi$ Her	15.9	1	$-12.70 \pm 0.15$	NGP	
220140	V368 Cep	19.7	1	$6.06 \pm 0.22$	LIC	
97334	MN UMa	21.7	1	$4.54 \pm 0.19$	LIC	
	WD1337+705	24.8	1	$1.67 \pm 0.32$	LIC	
222107	$\lambda$ And	25.8	1	$0.24 \pm 0.70$	NEW	Eri
			2	$4.81 \pm 0.24$	LIC	
			3	$10.27 \pm 0.21$	Hyades	
180711	$\delta$ Dra	30.7	1	$-1.78 \pm 0.14$	LIC	
12230	47 Cas	33.6	1	$10.076 \pm 0.071$	LIC	
163588	$\xi$ Dra	34.2	1	$-13.72 \pm 0.76$	Mic	
			2	$-6.27 \pm 0.42$	LIC	
216228	$\iota$ Cep	35.4	1	$2.93 \pm 0.18$	LIC	
93497	$\mu$ Vel	35.5	1	$-5.61 \pm 0.53$	G	
			2	$0.2 \pm 1.3$	Cet	
149499	V841 Ara	37.1	1	$-25.90 \pm 0.63$	Aql	
			2	$-19.56 \pm 0.91$	LIC	
			3	$-13.32 \pm 0.68$	NEW	Eri
210334	AR Lac	42.0	1	$-13.32 \pm 0.34$	NEW	
			2	$-0.63 \pm 0.33$	LIC	
28911	HIP21267	43.9	1	$14.30 \pm 0.26$	Hyades	
			2	$20.3 \pm 2.2$	Aur	
			3	$23.83 \pm 0.45$	LIC	
28677	85 Tau	44.9	1	$13.81 \pm 0.77$	Hyades	
			2	$18.6 \pm 1.1$	Aur	
			3	$23.26 \pm 0.36$	LIC	
204188	IK Peg	46.0	1	$-11.6 \pm 1.3$	Eri	
			2	$-6.72 \pm 0.24$	LIC	
	WD0549+158	49	1	$22.58 \pm 0.81$	LIC	
	WD2004-605	58	1	$-18.73 \pm 0.28$	Vel	
			2	$-12.06 \pm 0.79$	LIC	
9672	49 Cet	61.3	1	$10.15 \pm 0.70$	LIC	
			2	$13.69 \pm 1.4$	disk	G
43940	HR2265	62.1	1	$11.13 \pm 0.23$	Blue	
			2	$18.21 \pm 0.69$	Dor	
			3	$22.28 \pm 0.64$	NEW	
137333	$\rho$ Oct	66.6	1	$-8.82 \pm 0.59$	G	
			2	$-1.9 \pm 1.0$	Blue	
			3	$3.2 \pm 3.4$	Aql	NEW
			4	$9.61 \pm 0.57$	NEW	
3712	$\alpha$ Cas	70.1	1	$-6.49 \pm 0.36$	NEW	
			2	$-2.4 \pm 0.44$	NEW	
			3	$9.24 \pm 0.30$	LIC	
149382	HIP81145	76.5	1	$-32.73 \pm 0.31$	G	
			2	$-25.28 \pm 0.31$	Mic	
			3	$-16.4 \pm 1.7$	NEW	
	WD0621-376	78	1	$9.11 \pm 0.31$	Blue	
			2	$16.00 \pm 0.28$	Dor	
			3	$22.41 \pm 0.29$	NEW	
149730	R Ara	80.4	1	$-24.15 \pm 0.63$	Aql	
			2	$-19.3 \pm 1.8$	G	
			3	$-14.28 \pm 0.57$	NEW	Eri
			4	$-7.02 \pm 0.98$	NEW	Blue
			5	$-2.5 \pm 1.8$	NEW	
			6	$2.13 \pm 0.47$	NEW	
	IX Vel	96.3	1	$2.268 \pm 0.062$	LIC	NEW
			2	$4.91 \pm 0.37$	G	
			3	$16.44 \pm 0.32$	Vel	
			4	$20.80 \pm 0.73$	Cet	
75747	RS Cha	97.8	1	$-4.86 \pm 0.12$	G	
			2	$-1.40 \pm 0.11$	Vel	
			3	$10.64 \pm 0.12$	NEW	
			4	$17.27 \pm 0.11$	NEW	
141569	HIP77542	99.0	1	$-31.88 \pm 0.56$	NEW	
			2	$-27.55 \pm 0.15$	G	
			3	$-21.21 \pm 0.18$	Leo	Oph
			4	$-12.89 \pm 0.23$	NEW	
			5	$-6.0 \pm 1.1$	disk	NEW
			6	$2.84 \pm 0.44$	NEW	

Table 5.1 lists every component detected in this sample and the cloud with which it best agrees. If the component does not match any clouds, it is labeled “NEW.” The label “disk” denotes absorption by a circumstellar disk rather than ISM. In some cases, two explanations are reasonable to explain the absorption. The less likely one is listed in the “Alternative Explanation” column. The velocities listed are the weighted means of the velocities measured in MgII, FeII, and MnII unless one or both of the latter two are not detected. The MgII velocity is not used if the line is severely blended and saturated.

## 5.2 Finer Details

The LISM is not a homogenous structure (Frisch & York 1991; Diamond et al. 1995). Depending on the direction of observation, total column densities can vary more than an order of magnitude over the same distance Redfield & Linsky (2002). These changes are apparent over large angular scales, but to examine the finer structure requires sight lines with small angular separation. For example, Redfield & Linsky (2001) observed MgII in 18 stars in the Hyades, and were able to identify the signature of a second cloud (the Hyades Cloud) in 10 sight lines. These closely spaced sight lines also put tight constraints on cloud boundaries if different components are observed in each sight line. In this survey, two pairs of stars offer detail on a scale of  $<2^\circ$ .

V841 Ara and R Ara are separated by only  $0.5^\circ$ , but their distances are 37.1 pc and 80.4 pc respectively. The R Ara sight line shows three extra components, suggesting that three new clouds begin in the intervening 43.3 pc. It is also possible that the components begin in the  $0.5^\circ$  between the sight lines and are not constrained by the distance of V841 Ara, but this scenario is unlikely given that

this angular separation corresponds to 0.32 pc at the distance of R Ara. Both sight lines show nearly identical velocity structure for the three bluest components, two of which have been identified as the Aql Cloud and the LIC. The  $\sim -14 \text{ km s}^{-1}$  component seen in both sight lines appears to be a new cloud that begins within 37.1 pc. The three components seen only in R Ara likely belong to unidentified clouds that begin beyond 37.1 pc.

Separated by  $1.3^\circ$ , HD 43940 (62.1 pc) and WD0621-376 (78 pc) show three similar absorption components that agree in velocity. The two bluest components matched the model predictions for the Blue and Dor Clouds. The third component seems to be an unidentified cloud seen in both sight lines. The fact that no new component appears in the longer sight line shows that no new clouds with detectable column densities begin in the 16 pc span between the stars.

### 5.3 Temperature and Turbulence

This sample of Doppler parameters will be combined with MAST archive data of lighter ions along the same sight lines. With a similar data set, Redfield & Linsky (2004b) were able to identify the contributions of thermal and turbulent broadening to ISM line profiles by comparing lighter and heavier ions. Their 50 individual measurements yielded a weighted mean LISM gas temperature ( $T$ ) of 6680 K ( $\sigma = 1490 \text{ K}$ ) and weighted mean turbulent velocity ( $\xi$ ) of  $2.24 \text{ km s}^{-1}$  ( $\sigma = 1.03 \text{ km s}^{-1}$ ). Equation 4.1 in Chapter 4 shows the dependence of the Doppler parameter ( $b$ ) on  $T$  and  $\xi$ . For more massive ions, the contribution of thermal broadening to the Doppler parameter drops and the contribution of turbulence and unresolved clouds increases. The calculation of  $T$  and  $\xi$  has already been performed for the sight line towards  $\epsilon$  Ind (see Figure 5.1). The measured  $T$  and

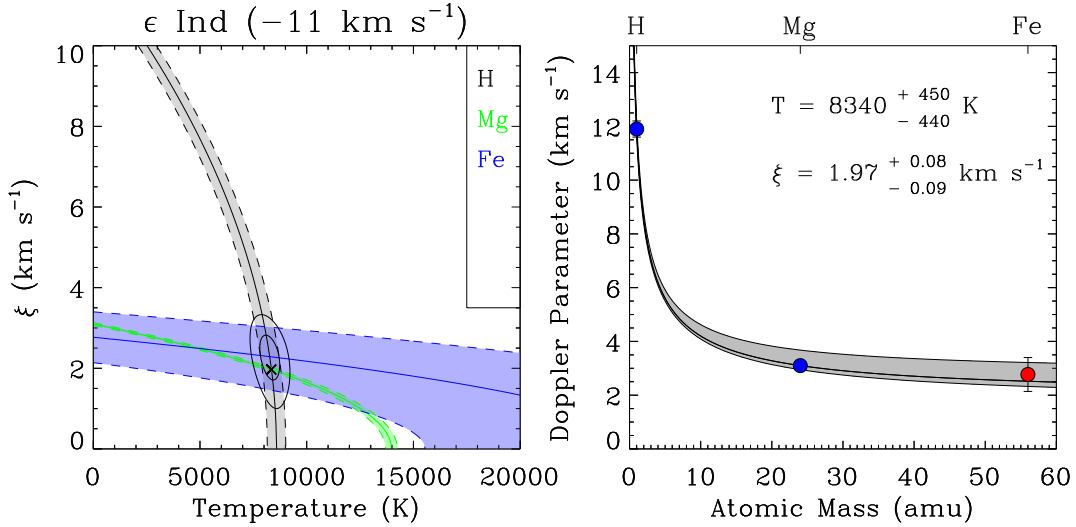


**Figure 5.1:** Determination of the temperature and turbulent velocity for the LISM absorption component observed towards  $\epsilon$  Ind. This measurement requires an observation of a light ion such as HI and a minimum of one other ion at least as heavy as MgII. On the left plot, the best-fit Doppler parameter for each ion is the solid line along with  $\pm 1\sigma$  error dashed lines, color coded according to the bar on the right. The black  $\times$  symbol marks the best-fit  $T$  and  $\xi$  given the  $b$  values of all the ions involved. Surrounding the  $\times$  symbol are  $\pm 1\sigma$  and  $\pm 2\sigma$  error contours. On the right, the Doppler parameter is plotted against atomic mass, with each point labeled at the top of the plot. A line of best-fit is shown with  $\pm 1\sigma$  error shown in gray.

$\xi$  agree with the Redfield & Linsky (2008) values for the LIC ( $T = 7500 \pm 1300$  K,  $\xi = 1.62 \pm 0.75$  km s<sup>-1</sup>). Future work will compare samples of light ions with this sample of heavy ions that have identical velocity components to differentiate  $T$  and  $\xi$  of LISM clouds.

## 5.4 Astrospheres

Knowledge of the LISM environment around a star is crucial to a complete understanding of its astrosphere. An astrosphere, analogous to the Sun’s heliosphere, marks the interface between the outward pressure of the stellar wind and the flow vector of the surrounding ISM. The astrosphere may expand or contract depending on the density of the ISM as well as the strength of the stellar wind. Wyman (2011) observed the LISM in the direction of the Sun’s historical line of motion in order to investigate how it may have impacted the heliosphere and the secondary effects on Earth’s climate. The ISM environment of a star may achieve densities great enough to compress the astrosphere to within the orbit of planets, exposing their atmospheres directly to the ISM and the full brunt of the Galactic cosmic ray flux.

To detect an astrosphere, one may look for the spectral signature of its “hydrogen wall.” When ISM neutrals interact with ions from the solar wind, they experience charge exchange, producing an abundance of neutral hydrogen (Wood et al. 2004). This hydrogen builds up at the interface of the stellar wind and the ISM, and as a result, produces a deep, broad Ly $\alpha$  absorption feature. The feature is often highly saturated and difficult to differentiate from interstellar H absorption. Observing heavy ions in the same direction provides important constraints on analysis of heliospheric and astrospheric HI absorption by measuring the number and velocity of the LISM components.

Observations of Ly $\alpha$  towards  $\epsilon$  Ind and  $\lambda$  And led Wood et al. (1996) to conclude that, for both sight lines, an astrospheric HI absorption component was necessary to explain a width and velocity discrepancy between the HI and DI absorption lines. For each sight line, they identified one LISM component and

an astrospheric component. Assuming  $\xi = 1.2 \text{ km s}^{-1}$ , they measured an LISM temperature  $T = 8500 \pm 500 \text{ K}$  for  $\epsilon \text{ Ind}$  and  $T = 11,500 \pm 500 \text{ K}$  for  $\lambda \text{ And}$ . The  $\lambda \text{ And}$  LISM temperature was high, suggesting that the large  $\text{Ly}\alpha$  feature contained blends.

MgII and FeII have both been observed towards  $\epsilon \text{ Ind}$  and  $\lambda \text{ And}$ , allowing for a more detailed look at the LISM velocity structure towards the two stars. The  $\epsilon \text{ Ind}$  sight line contains only one absorption component for both MgII and FeII, confirming the conclusions of Wood et al. (1996). Furthermore, the Doppler parameters indicate that  $\xi = 1.97_{-0.09}^{+0.08} \text{ km s}^{-1}$ , a higher value than was assumed. The temperature measurement remains consistent. My examination of the MgII and FeII absorption lines towards  $\lambda \text{ And}$ , however, reveals that there are three LISM components, not one. Therefore, the Doppler parameter determined solely through  $\text{Ly}\alpha$  absorption is artificially broadened, leading to an overestimation of the LISM  $T$  and  $\xi$ .

In light of these new results, the  $\text{Ly}\alpha$  towards  $\lambda \text{ And}$  was refit with the assumption that the velocity spacing of the three ISM components matched that of the MgII components (B. Wood, private communication). Fits were attempted with and without an astrospheric contribution. Figure 5.2 shows the best ISM-only fit, which assumes the same column density ratios as the MgII fit but varies the Doppler parameters. The fit achieved a  $\chi^2_\nu$  of 1.21 but resulted in the first component having a very large ISM cloud temperature ( $T \sim 18,000 \text{ K}$ ). Adding an astrospheric absorption component reduced this value and slightly improved the  $\chi^2_\nu$  to 1.19 (Figure 5.3). Still, the severely blended ISM components prevent any confident measurement of the HI and DI  $b$  and  $N$  values. Ultimately, the information from the MgII and FeII absorption does not preclude the presence of an astrosphere.

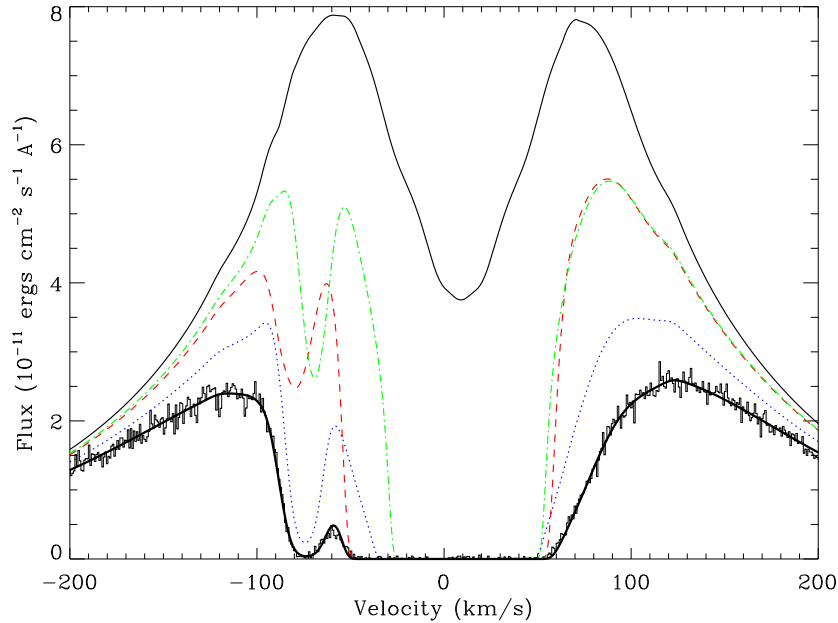


**Figure 5.2:** A fit of the Ly $\alpha$  line towards  $\lambda$  And incorporating three ISM components and no astrospheric component ( $\chi^2_\nu = 1.21$ ). The ISM profiles have trouble matching the slope along the blue side of the HI feature, suggesting that an astrospheric component may be necessary to model this profile.

## 5.5 Circumstellar Disks

Narrow absorption features in stellar spectra are usually the signature of foreground interstellar absorption, but in rare cases, they may also result from material in a circumstellar (CS) disk. CS disks evolve through phases classified by their primordial gas-to-dust ratio. Primordial disks generally exist around pre-main sequence stars where accretion of disk material is still occurring and possess massive, optically thick gas-rich disks. Transitional disks have optically thin inner regions and optically thick outer regions as indicated by mid- to far-IR excesses but little to no near-IR excess. Sub-millimeter CO emission indicates that these outer regions are gas rich (e.g., Qi et al. 2004). Approximately  $10^7$  years into the star's lifetime, the primordial material clears, and the now main sequence star

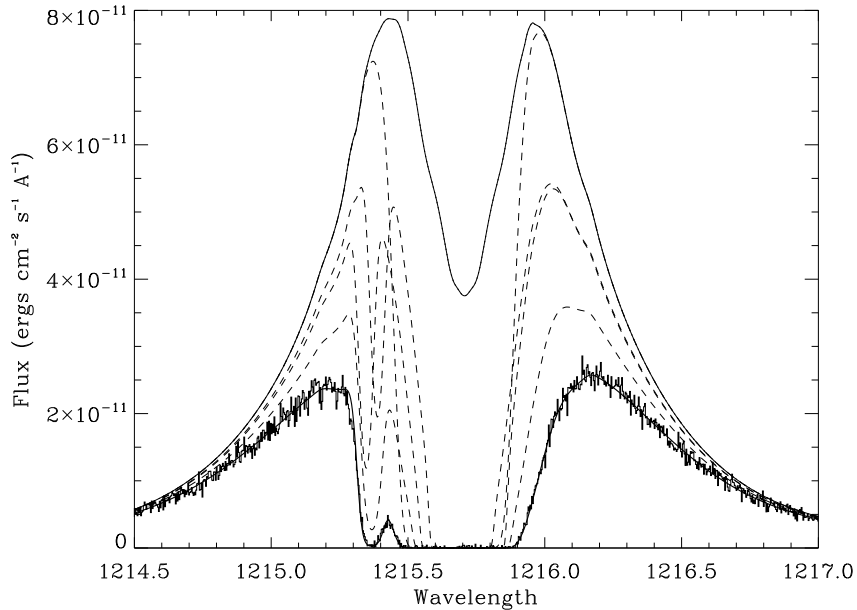


**Figure 5.3:** A fit of the Ly $\alpha$  line towards  $\lambda$  And incorporating three ISM components and an astrospheric component ( $\chi^2_{\nu} = 1.19$ ).

is surrounded by a gas-poor debris disk. Mechanisms that remove gas from the system include the formation of a gas giant planet, depletion onto dust grains, and photoevaporation by the central star.

UV and optical spectroscopy have been used to detect small amounts of gas in debris disks (e.g., Laganage et al. 1998; Chen & Jura 2003). This gas is not primordial, but rather, the result of collisions and evaporation of planetesimals (Roberge & Weinberger 2008). Detecting gas in the debris disk of a star is challenging because very little gas exists. It requires sensitive observation of nearby, edge-on systems. The A star  $\beta$  Pictoris, which satisfies these prerequisites, has become the canonical example of a well-characterized gas disk. UV and optical observations have indicated roughly solar abundances of gaseous elements with the exception of a large overabundance of carbon (Roberge et al. 2006). Similar characterizations of other CS disk systems will enable better understanding of

planet formation and composition.

### 5.5.1 Sight lines towards stars with CS disks

Two stars observed in this survey are known to possess CS disks. Each of their spectra show multiple narrow absorption features, one of which may be CS. To differentiate an ISM component from a CS one, it is useful to compare the radial velocity of the star to that of the absorbing material. If the two coincide, the material may originate from a stable CS disk, but it is then necessary to check nearby sight lines. If nearby sight lines show a similar feature or a kinematic model of the LISM predicts a cloud with the same projected velocity, then it strongly suggests it is not CS. There is, however, a chance that CS absorption is blended with ISM absorption.

#### 49 Cet

One particular sight line of interest is towards 49 Cet, an A1V star 61.3 pc away (van Leeuwen 2007). 49 Cet shows an infrared excess indicative of circumstellar dust grains (Sadakane & Nishida 1986). Further observations indicate the disk is in the rare transitional phase in which the inner disk is cleared of silicate dust grains while the outer disk is not (Zuckerman et al. 1995; Dent et al. 2005). CO observations show an extended molecular gas distribution that is approximately edge-on with a heliocentric velocity of  $12.2 \pm 1.0 \text{ km s}^{-1}$  (Hughes et al. 2008).

Two partially blended, narrow absorption features were detected along the line of sight ( $v_{\text{MgII}} = 9.0 \pm 1.3 \text{ km s}^{-1}$ ,  $14.4 \pm 1.1 \text{ km s}^{-1}$  ;  $v_{\text{FeII}} = 11.0 \pm 1.6 \text{ km s}^{-1}$ ,  $13.65 \pm 0.15 \text{ km s}^{-1}$ ). Given the presence of an optically thin, gas rich disk around 49 Cet, it may be possible that the disk produces one of the components.

When compared to the dynamical model both components agree with the LIC predicted along the line of sight ( $v_{\text{LIC}} = 11.00 \pm 1.29 \text{ km s}^{-1}$ ), though the first component agrees better. The second component ( $\sim 14 \text{ km s}^{-1}$ ) agrees with the velocity vector of the nearby G cloud ( $v_{\text{G}} = 16.95 \pm 1.64 \text{ km s}^{-1}$ ), but only within  $3\sigma$  of zero. The heliocentric velocity of 49 Cet agrees well with the second component. It seems this component is indeed from the disk. As of this writing, there are no nearby sight lines that can be used to rule out ISM absorption as the source of the second component.

### HD 141569

The sight line towards HD 141569 is the longest sight line in the sample (99 pc). As expected, the absorption in its direction is deep and complicated. Six components were observed in MgII, four of which are saturated, as well as five components in FeII, and four in MnII. HD 141569 is a B9.5V Herbig Ae/Be star (Jaschek & Jaschek 1992). Spectral energy distribution (SED) observations indicate a large ( $\sim 400 \text{ AU}$ ) circumstellar disk inclined by  $51 \pm 3^\circ$  (Weinberger et al. 1999). Dent et al. (2005) measured a radial velocity of  $-7.6 \pm 0.3 \text{ km s}^{-1}$  using the disk's double-peaked CO  $J = 2 - 1$  spectral profile.

Of the six components detected in MgII, only two can be explained by known ISM clouds. The remaining four may be clouds that are currently unidentified, but observations of nearby stars are required to produce a velocity vector. The  $-5.5 \text{ km s}^{-1}$  component agrees with the heliocentric velocity of HD 141569, so it appears to be CS absorption. Other  $\geq 99 \text{ pc}$  sight lines should be observed to confidently rule out ISM components.

### 5.5.2 Sight lines near a star with a CS disk

Two sight lines in the SNAP survey probe the region close to HD 32297. HD 32297 is an A0V star at 112 pc with an edge-on debris disk (Schneider et al. 2005). Redfield (2007) observed NaI in the optical toward HD 32297 and several nearby stars, all of which shared a LIC absorption component. Only for HD 32297, however, was a second absorption component detected, consistent with its  $\sim 20$  km s<sup>-1</sup> radial velocity. Five observations of HD 32297 over 5 months showed the same two components, confirming that this unique component was in fact NaI gas absorption in the stable edge-on debris disk.

Both HD 28911 (9.0° separation from HD 32297) and 85 Tau (11.2° separation) show similar absorption components to each other, confirming the Redfield & Linsky (2008) kinematic model prediction that three discrete clouds (LIC, Aur, Hyades) begin before 43.9 pc in their direction. Two ISM components were observed in MgI, MgII, MnII, ZnII, FeI, and FeII towards HD 32297 (Fusco et al. 2013) and they agree with the  $\sim 19$  km s<sup>-1</sup> and  $\sim 23.8$  km s<sup>-1</sup> components I observe in the nearby stars. However, the  $\sim 20$  km s<sup>-1</sup> disk component is likely coincidental because it is not detected in other stars with smaller angular separation from HD 32297. Only the LIC extends between 85 Tau, HD 28911, and HD 32297. The Aur and Hyades clouds must terminate somewhere between HD 32297 and the 85 Tau/HD 28911 region.

# Chapter 6

## Conclusions

High-resolution NUV observations of 34 broadly distributed stars within 100 pc have revealed widespread MgII, FeII, and MnII absorption in the LISM. Among all the sight lines, 76 MgII components, 71 FeII components, and 4 MnII components were detected. Each FeII and MnII component matches an MgII component to within  $3 \text{ km s}^{-1}$  in radial velocity, evidence that they arise from the same LISM clouds. The distribution of velocities are consistent with the bulk flow of the cluster of local interstellar clouds, and the Doppler parameters reflect the greater contribution of thermal broadening on the lighter MgII ion. The average number of components per sight line remains flat after 10 pc and begins rising beyond  $\sim 60$  pc, evidence that denser regions of clouds surround the solar system and trace the edge of the Local Bubble.

Every prediction made by the Redfield & Linsky (2008) kinematic model of the LISM was confirmed by an observed component. The success of this model points to the value of these observations in understanding the velocity structure of the LISM. Many components not predicted along the line of sight agree with the projected velocities of nearby clouds. In these cases, the cloud boundaries will need to be redrawn. For longer sight lines, many unidentified clouds were detected. These can be compared to nearby sight lines to construct a velocity vector.

Two stars in the sample have known circumstellar disks. 49 Cet, which has an edge-on debris disk, shows MgII, FeII, and MnII absorption with coincident velocity to the star. Likewise, MgII and FeII components towards HD 141569 share the same radial velocity as the star. In both sight lines, these components agree better with the star’s radial velocity than any model cloud predictions. To confidently eliminate the possibility that this absorption is from the ISM will require further examination of nearby sight lines.

Clouds detected towards  $\epsilon$  Ind and  $\lambda$  And were of particular interest because these stars show evidence of astrospheres. Understanding the LISM cloud velocity structure in the foreground of these stars informs the fitting of the often blended and saturated Ly $\alpha$  lines used to detect astrospheres. The  $\epsilon$  Ind sight line shows only one cloud, which was assumed in the original Ly $\alpha$  fitting. On the other hand, three components were detected towards the  $\lambda$  And sight line, which was previously fit under the assumption of one high temperature cloud. The Ly $\alpha$  line was reanalyzed with three ISM clouds included in the fit. An astrosphere detection is still viable, but the interstellar HI properties are poorly constrained.

## 6.1 Future Work

The results presented here are only the beginning in a series of investigations that will characterize the LISM and its constituent clouds. When combined with spectra of lighter ions in the MAST archive, it will be possible to measure the temperature and turbulence of LISM clouds as was shown with the LIC towards  $\epsilon$  Ind. Furthermore, observations of different ionization stages of Mg, Fe, and Mn along the same sight lines can help describe the interstellar radiation field. Similarly, a comparison of column densities of various ions and across many sight lines

---

provides a valuable inventory of the abundances and depletions of LISM clouds. With more sight lines, tighter constraints can be put on the three dimensional morphology of the LISM. Certain stars in the sample with small angular separations already tighten the edges of clouds in three dimensions. When this sample is incorporated into the LISM dynamical model, it may lead to the identification of new clouds and will at minimum increase the accuracy of the model's predictions.

# Bibliography

- Ayres, T. R. 2010, *ApJS*, 187, 149
- Bacon, F. 1626, *Sylva Sylvarum: Or Naturall Historie*. In *Ten Centuries* (William Lee), 95
- Beals, C. S. 1936, *MNRAS*, 96, 661
- Bevington, P. R. 2003, *Data Reduction and Error Analysis for the Physical Sciences* (McGraw-Hill)
- Chen, C. H., & Jura, M. 2003, *ApJ*, 582, 443
- Cowie, L. L., & Songaila, A. 1986, *ARA&A*, 24, 499
- Dent, W. R. F., Greaves, J. S., & Coulson, I. M. 2005, *MNRAS*, 359, 663
- Diamond, C. J., Jewell, S. J., & Ponman, T. J. 1995, *MNRAS*, 274, 589
- Frisch, P. C., Grodnicki, L., & Welty, D. E. 2002, *ApJ*, 574, 834
- Frisch, P. C., Redfield, S., & Slavin, J. D. 2011, *ARA&A*, 49, 237
- Frisch, P. C., & York, D. G. 1991, in *Extreme Ultraviolet Astronomy*, ed. R. F. Malina & S. Bowyer, 322
- Fusco, M., Redfield, S., Roberge, A., Stapelfeldt, K. R., & Jensen, A. G. 2013, in *American Astronomical Society Meeting Abstracts*, Vol. 221, American Astronomical Society Meeting Abstracts, 144.20

- Genova, R., Beckman, J. E., Molaro, P., & Vladilo, G. 1990, *ApJ*, 355, 150
- Gontcharov, G. A. 2006, *Astronomy Letters*, 32, 759
- Hartmann, J. 1904, *ApJ*, 19, 268
- Heger, M. L. 1919, *PASP*, 31, 304
- Holberg, J. B., Barstow, M. A., & Sion, E. M. 1998, *ApJS*, 119, 207
- Hughes, A. M., Wilner, D. J., Kamp, I., & Hogerheijde, M. R. 2008, *ApJ*, 681, 626
- Jaschek, C., & Jaschek, M. 1992, *A&AS*, 95, 535
- Jenkins, E. B. 1987, in *Astrophysics and Space Science Library*, Vol. 134, *Interstellar Processes*, ed. D. J. Hollenbach & H. A. Thronson, Jr., 533–559
- Lagrange, A.-M., Beust, H., Mouillet, D., Deleuil, M., Feldman, P. D., Ferlet, R., Hobbs, L., Lecavelier Des Etangs, A., Lissauer, J. J., McGrath, M. A., McPhate, J. B., Spyromilio, J., Tobin, W., & Vidal-Madjar, A. 1998, *A&A*, 330, 1091
- Lallement, R., & Bertin, P. 1992, *A&A*, 266, 479
- Lallement, R., Ferlet, R., Lagrange, A. M., Lemoine, M., & Vidal-Madjar, A. 1995, *A&A*, 304, 461
- Lallement, R., Welsh, B. Y., Vergely, J. L., Crifo, F., & Sfeir, D. 2003, *A&A*, 411, 447
- Linsky, J. L., Rickett, B. J., & Redfield, S. 2008, *ApJ*, 675, 413

- Mathis, J. S. 1987, in *Astrophysics and Space Science Library*, Vol. 129, Exploring the Universe with the IUE Satellite, ed. Y. Kondo, 517–529
- McCray, R. A. 1987, in *Spectroscopy of Astrophysical Plasmas*, ed. A. Dalgarno & D. Layzer, 255–278
- McKee, C. F., & Ostriker, J. P. 1977, *ApJ*, 218, 148
- Morton, D. C., & Spitzer, Jr., L. 1966, *ApJ*, 144, 1
- Qi, C., Ho, P. T. P., Wilner, D. J., Takakuwa, S., Hirano, N., Ohashi, N., Bourke, T. L., Zhang, Q., Blake, G. A., Hogerheijde, M., Saito, M., Choi, M., & Yang, J. 2004, *ApJL*, 616, L11
- Redfield, S. 2007, *ApJL*, 656, L97
- Redfield, S., & Linsky, J. L. 2001, *ApJ*, 551, 413
- . 2002, *ApJS*, 139, 439
- . 2004a, *ApJ*, 602, 776
- . 2004b, *ApJ*, 613, 1004
- . 2008, *ApJ*, 673, 283
- Roberge, A., Feldman, P. D., Weinberger, A. J., Deleuil, M., & Bouret, J.-C. 2006, *Nature*, 441, 724
- Roberge, A., & Weinberger, A. J. 2008, *ApJ*, 676, 509
- Sadakane, K., & Nishida, M. 1986, *PASP*, 98, 685
- Schneider, G., Silverstone, M. D., & Hines, D. C. 2005, *ApJL*, 629, L117

- Sembach, K. R., & Savage, B. D. 1992, *ApJS*, 83, 147
- Sfeir, D. M., Lallement, R., Crifo, F., & Welsh, B. Y. 1999, *A&A*, 346, 785
- Slavin, J. D., & Frisch, P. C. 2008, *A&A*, 491, 53
- van Leeuwen, F. 2007, *A&A*, 474, 653
- Weinberger, A. J., Becklin, E. E., Schneider, G., Smith, B. A., Lowrance, P. J.,  
Silverstone, M. D., Zuckerman, B., & Terrile, R. J. 1999, *ApJL*, 525, L53
- Wood, B. E., Alexander, W. R., & Linsky, J. L. 1996, *ApJ*, 470, 1157
- Wood, B. E., Müller, H.-R., Zank, G. P., Izmodenov, V. V., & Linsky, J. L. 2004,  
*Advances in Space Research*, 34, 66
- Wood, B. E., Redfield, S., Linsky, J. L., & Sahu, M. S. 2002, *ApJ*, 581, 1168
- Wyman, K. 2011, Master's thesis, Wesleyan University
- Zuckerman, B., Forveille, T., & Kastner, J. H. 1995, *Nature*, 373, 494